Experimental evaluation of hydrothermal performance in airfoil-fin PCHE with supercritical pressure hydrocarbon fuel

Weitong Liu [a,b,c], Guoqiang Xu [a,b,c], Haoxing Zhi [b], Ruoyu Wang [a,b], Mowen Li [d], Yanchen Fu [a,b,c,*]

[a] Tianmushan Laboratory, Hangzhou 310023, China
[b] Research Institute of Aero-engine, Beihang University, Beijing 100191, China
[c] Collaborative Innovation Center for Advanced Aero-Engine, Beihang University, Beijing 100191, China
[d] Beijing Power Machinery Institute, Beijing 100074, China

ARTICLE INFO

ABSTRACT

The printed circuit heat exchanger (PCHE) stands out as a promising candidate for thermal systems. However, experimental studies on the thermodynamic performance of airfoil-fin PCHE using supercritical pressure hydrocarbon fuel are scarce, and reliable methods for calculating the Nusselt number (Nu) remain underdeveloped. Therefore, this work presents an experimental investigation of the thermal-hydraulic performance of an airfoil-fin PCHE, using supercritical pressure hydrocarbon fuel and water as working fluids. The correlations for Nu and friction coefficient (f) were developed, with deviations of ± 8 % for f and ± 20 % for Nu. Under laminar flow conditions, the airfoil-fin PCHE demonstrated a high f, being 2.93 times greater than that of the straight PCHE. The heat transfer superiority of the airfoil-fin PCHE compared to other channel types depends on Re. When $Re > 334$, the airfoil-fin PCHE shows the best heat transfer performance, exhibiting an average Nu that is 7.74 times higher than the straight PCHE, 3.15 times higher than the zigzag PCHE, and 1.65 times higher than the S-shaped PCHE. The overall thermodynamic performance of the airfoil-fin PCHE also improves with increasing Re. Additionally, a comparative assessment of six different Nu calculation and fitting methods has been conducted based on experimental results.

1. Introduction

As advanced energy and power systems continue to progress rapidly, there is an increasing need for heat transfer technologies that are more efficient, compact, and stable. The efficiency and reliability of energy, power, and propulsion systems are of utmost importance, and heat exchangers are pivotal in this regard. Serving as key components, they play critical roles in transferring thermal energy and can function as heaters, precoolers, condensers, and recuperators. The Printed circuit heat exchanger (PCHE) stands out as a promising candidate compared to traditional heat exchangers like tube-shell, plate-fin, tube-fin types, and others. Its notable features include high compactness, efficiency, and remarkable reliability, especially under harsh conditions such as high temperature and pressure [1]. Currently, PCHE has been successfully employed in many fields, including high-temperature gas-cooled reactors [2], concentrated solar power plants [3], supercritical CO_2 (sCO_2) Braton cycle [4,5], waste heat recovery systems [6,7], floating liquefied natural gas devices [8], etc. Moreover, PCHE also has broad application prospects in various fields such as next-generation nuclear power conversion systems [9], aero-engine thermal management systems [10–12], hydrogen energy [13], and so on.

The fabrication of PCHE involves photochemical etching and diffusion bonding techniques, forming microchannels with various structures. The channel shapes in PCHE are currently designed in four primary configurations: straight, zigzag, S-shape, and airfoil. Extensive research has been conducted to investigate the thermal-hydraulic performance of PCHEs under various channel configurations. Chen et al. [14] used a dynamic model to predict and analyze the transient and steady performance of a straight-channel PCHE, comparing the result with experimental data. Liu et al. [15] experimentally analyzed the heat transfer characteristics between water and sCO_2 in counter flow direction in a straight-channel PCHE, indicating heat transfer enhancement occurred when CO_2 changed from the gas-like region to the pseudo-critical region. Seo et al. [16] carried out performance tests for a straight microchannel PCHE with water and developed heat transfer and

---

* Corresponding author at: Research Institute of Aero-engine, Beihang University, Beijing 100191, China.
  E-mail address: yanchenfu@buaa.edu.cn (Y. Fu).

Nomenclature

A	heat transfer area of HEX [m^2]
A_c	cross-sectional area [m^2]
a	coefficient
b	coefficient
C	coefficient
c_p	isobaric specific heat capacity [J/(kg·K)]
d	hydraulic diameter [mm]
f	friction coefficient
h	heat transfer coefficient [W/(m^2·K)]
K	overall heat transfer coefficient [W/(m^2·K)]
L_{core}	distance between the core inlet and core outlet [mm]
L_{fin}	chord length of the airfoil fin [mm]
L_v	vertical pitch [mm]
L_h	horizontal pitch [mm]
L_s	staggered pitch [mm]
m	mass flow rate [kg/s]
Nu	Nusselt number
Pr	Prandtl number
P	pressure [MPa]
ΔP	pressure drop [kPa]
P_{fin}	end face perimeter of the fin [mm]
Q	heat transfer rate [W]
R	The overall thermal resistance of PCHE [K/W]
Re	Reynolds number
S	The side surface area of the element [m^2]
S_{top}	The top surface area of the fin [mm^2]
T	temperature [°C]
ΔT_m	logarithmic mean temperature difference [°C]
u	velocity [m/s]
V	The volume of the element [m^3]

Greek symbols

Δ	difference
δ	wall thickness [mm]
σ	minor loss coefficient
μ	dynamic viscosity [μPa·s]
λ	thermal conductivity [W/(m·K)]
ε	fit deviation [%]

Subscripts

ave	average
core	PCHE core
c	cold fluid
h	hot fluid
fin	airfoil fin
in	inlet
out	outlet
cal	calculated data
exp	experimental data
ref	reference
w	wall
water	water
fuel	Chinese aviation kerosene RP-3

Abbreviations

CFD	Computational Fluid Dynamics
HTC	Heat transfer coefficient
PCHE	Printed circuit heat exchanger
PEC	Performance evaluation criteria
sCO$_2$	Supercritical CO$_2$
GA	Genetic Algorithm
NACA	National Advisory Committee for Aeronautics

pressure drop empirical correlations. PCHE with S-shaped fins and zigzag fins was explored by Ngo et al. [17]. The results demonstrated that the Nusselt number (Nu) of the S-shaped PCHE is 24 %–34 % lower than that of the zigzag PCHE, while the friction coefficient (f) is reduced by 4–5 times. In the research of Kim et al. [18,19] they performed experimental and numerical investigation on the zigzag PCHE and proposed the local pitch-averaged and single correlations of Nu and Fanning factor. Yoon et al. [20] established the Nu and f correlations incorporating geometric parameters using Computational Fluid Dynamics (CFD) for laminar flow in zigzag PCHE. Katz et al. [21] employed the constrained nonlinear multi-variable method to develop the heat transfer correlation for SCO$_2$ within zigzag PCHE in the Reynolds number (Re) range of 500–18,000. On the basis of the measurement of temperature at various points along the zigzag channel, Jin et al. [22] explored the impact of inlet temperature, system pressure, and mass flux on the heat transfer performance of sCO$_2$ in PCHE. The thermodynamic performance of water flowing within PCHE with different sinusoidal wavy channels was investigated numerically by Qu et al. [23], suggesting a structure with increased cycle groups and smaller amplitudes in the inlet to achieve better overall performance. Samarmad and Jaffal [24] proposed PCHE with backward/forward-facing wavy channels, which is a combination of a U-shape path in the vertical planed and a wave path in the horizontal plane. Using water as the working fluid, the results demonstrated that the proposed structure has an improvement in Nu, with a slight increase in pressure drop. Samarmad and Jaffal [25] also designed a novel two-way corrugated channel PCHE. The proposed PCHE design was numerically and experimentally investigated with water as the working medium for both sides, indicating that the use of two-way corrugated channels is an effective technique for improving the performance evaluation factor, effectiveness, and Nu. Since the airfoil-

fin PCHE exhibits the best overall thermodynamic behavior [26,27], studies on it represent a growing field. Chou et al. [28] conducted a numerical analysis of PCHE incorporating multistage Tesla valves with geometric flow baffles using water as the working fluid. Results suggested that the Tesla valve configuration has a notable enhancement in thermal effectiveness. The effects of structure parameters of the airfoil fins on the thermal-hydraulic performance of sCO$_2$ within airfoil-fin PCHE have been conducted by Li et al. [29], suggesting the maximum thickness of the airfoil in the front for better performance. Tong et al. [30] carried out a numerical investigation on the thermodynamic performance of supercritical LNG in an airfoil-fin PCHE under rolling conditions, indicating better comprehensive performance as the rolling amplitude increased. Park and Kim [31] compared the performance between airfoil-fin PCHE and wavy PCHE through experiments using sCO$_2$, it has been found that the pressure drop in the wavy PCHE is 15 times that of the airfoil-fin PCHE. Chang et al. [32] designed an asymmetric airfoil and quantitatively evaluated the impact of flow direction on the comprehensive characteristics of the PCHE. In the research of Yang et al. [33], an analysis was conducted on a rhombic-fin PCHE performance, taking into account the combined influences of physical properties and turbulent intensity of sCO$_2$. Besides, the genetic algorithm (GA) was used to develop the Nu correlation.

In conclusion, these studies support the notion that high-precision correlations for heat transfer and pressure drop are crucial for designing PCHEs, especially the fitting of Nu correlations. However, there are indeed many challenges and nuanced issues in the calculation and fitting of Nu correlations. The following will elaborate on this matter.

Table 1 illustrates the representative experimental studies on the calculation and fitting methods of Nu in PCHEs. As is well known, Nu

Table 1

Representative experimental studies on the calculation and fitting methods of *Nu* in PCHEs.

Reference	Channel shape	Working fluid	Measure wall temperature or not	*Nu* calculation method and heat transfer correlation fitting method
Chen et al. [14]	Straight	Helium	No	Assuming *Nu* correlations are the same for the cold and hot sides, nonlinear regression is used to solve the two unknown constants.
Liu et al. [15]	Straight	sCO$_2$ Water	Yes	Direct calculation of *Nu* based on wall temperature.
Seo et al. [16]	Straight	Water	No	Modified Wilson plot method to obtain HTC, multiple linear regression is used to solve constants.
Park et al. [37]	Straight	sCO$_2$ Water	No	Seo correlation [16] is employed for the water side, then *Nu* on the sCO$_2$ side is computable.
Shin et al. [38]	Straight	Nitrogen	No	Gnielinski correlation is employed for the hot side, and then *Nu* on the cold side is computable.
Han et al. [39]	Straight	sCO$_2$ Water	No	Combined with CFD and experiments, *Nu* can be directly obtained.
Ngo et al. [17]	S-shaped Zigzag	CO$_2$	No	Assuming *Nu* correlations are the same for the cold and hot sides, the least-squares method is used to solve the three unknown constants.
Kim et al. [18,19]	Zigzag	Helium Water Mixture gas	No	Combined with CFD and experiments, *Nu* can be directly obtained.
Baik et al. [40]	Zigzag	sCO$_2$ Water	No	Combined with CFD and experiments, *Nu* can be directly obtained.
Katz et al. [21]	Zigzag	sCO$_2$ Helium	Yes	A constrained nonlinear multi-variable function solver is employed to solve the four unknown constants using an interior-point search algorithm.
Jin et al. [22]	Zigzag	sCO$_2$ Water	Yes	Direct calculation of *Nu* based on wall temperature.
Pidaparti et al. [34]	Airfoil Rectangular	sCO$_2$ Water	Yes	Direct calculation of *Nu* based on wall temperature.
Wang et al. [41]	Airfoil Straight	Molten salt Synthetic oil	No	Gnielinski correlation is used for the straight-fin side, then *Nu* on the airfoil-fin side is computable.
Shi et al. [42]	Airfoil Straight	Molten salt sCO$_2$	No	Combined with CFD and experiments, *Nu* can be directly obtained.
Han et al. [43]	Airfoil	Flue gas Water	No	Hausen equation [44] is used for the water side, and then *Nu* on the other side is obtained through experimental and numerical data.
Chang et al. [32]	Airfoil	CO$_2$ Water	No	First obtaining water-side HTC by water-water experiment, then *Nu* on the CO$_2$ side is computable.
Chung et al. [27]	Airfoil Straight	Nitrogen	No	Gnielinski correlation is used for the straight-

Table 1 (*continued*)

Reference	Channel shape	Working fluid	Measure wall temperature or not	*Nu* calculation method and heat transfer correlation fitting method
Park et al. [31]	Airfoil Straight	CO$_2$ Water	No	channel side, then *Nu* on the airfoil-fin side is computable. Seo correlation [16] is employed for the water side, then *Nu* on the sCO$_2$ side is computable.
Yang et al. [33]	Rhombic	sCO$_2$	No	GA is used to solve the seven unknown constants.

needs to be calculated through the heat transfer coefficient (HTC), which is directly related to heat flux, fluid bulk temperature, and inner wall temperature. For experimental studies on the thermal-hydraulic performance of PCHEs, heat flux and fluid bulk temperature can be indirectly calculated by measuring fluid mass flow rate, inlet, and outlet temperature. Nevertheless, due to the integral and complex nature of PCHE structures, precise measurement of wall temperatures in PCHEs can be challenging. Although some studies [15,21,22,34] in the existing literature have achieved wall temperature measurements, they typically measure temperatures not directly on the inner wall surface. And there is still a small distance between the temperature measurement point and the channel wall. The complex structure of PCHE channels makes thermal analysis challenging, and currently, there is a lack of research on theoretically deriving and calculating inner wall temperatures. Therefore, substituting the measured wall temperatures for the temperatures directly on the inner wall surface of the channels may lead to significant deviations in the calculation of the HTC, which is not conducive to the accurate calculation of the *Nu*. Moreover, some studies [16] employed the Wilson plot method [35] to determine the fluid HTC for the PCHE. The Wilson plot method has been well-established in the application of shell-and-tube heat exchangers and plate-fin heat exchangers, with numerous studies demonstrating its reliability. For straight PCHE, due to its similarity to shell-and-tube heat exchanger, the applicability of the Wilson plot method is expected. However, for heat exchangers with complex channel structures, such as airfoil-fin PCHEs, there is a lack of research demonstrating the applicability and reliability of using the Wilson plot method to determine HTC. Besides, the combination of numerical simulation and experiment to determine the *Nu* of the fluid inside a PCHE is a viable approach. Comparing experimental data with simulation results, the numerical simulation results are valid if the deviations are tiny. However, for structurally complex and large-sized PCHEs, the number of grids required can be immense. Due to the limited computational capacity of CFD, if it's not feasible to achieve a 1:1 simulation for a single channel and only partial channel simulations are conducted, the accuracy of the *Nu* obtained from numerical simulations cannot be guaranteed. Finally, since the overall heat transfer coefficient (*K*) of PCHE can be easily calculated from experimental data, some studies [17–19,21,33] directly use nonlinear multi-variable regression methods, GA, or other optimization algorithms to fit *Nu* correlations. However, if the number of constants to be determined is above 3, using these optimization algorithms to obtain fitting results may have problems [36]. On the one hand, the results of certain algorithms may depend on the initial values provided during the calculation. Different initial values can yield different results, potentially leading to an infinite set of solutions. While each solution may result in a small deviation in the *K* calculation for this PCHE, the *Nu* results for the cold and hot side fluids will be entirely different. In other words, this method only considers minimizing the fitting residual of the *K*, without taking into account the actual HTC for the cold and hot side fluids. On the other hand, even if some algorithms do not require initial values and have a unique set of solutions (such as GA), they may still face the aforementioned problems. The HTC obtained from the optimization algorithms

for the cold and hot side fluids may not represent their actual HTC, potentially leading to significant deviations when applying the *Nu* correlation of a single fluid to the design of other PCHEs.

The review of existing studies reveals a significant research gap in the evaluation of *Nu* calculation and fitting methods for experimental studies of PCHEs. Moreover, to the best of the author's knowledge, there is no existing research in the literature on the experimental study of thermal-hydraulic characteristics of supercritical pressure hydrocarbon fuel in airfoil-fin PCHEs. This absence of research limits the application of PCHEs in aero engine thermal management systems. Therefore, this study aims to evaluate *Nu* calculation and fitting methods in experimental research on airfoil-fin PCHEs and to explore the thermodynamic performance of supercritical pressure hydrocarbon fuel within airfoil-fin PCHE, aiming to provide guidance for the high-precision design of PCHEs. A PCHE equipped with NACA0025 airfoil fins has been designed and manufactured. Extensive experimental investigations were conducted to assess the thermal-hydraulic performance using water and supercritical pressure hydrocarbon fuel as working fluids. Finally, a comparative assessment of six different *Nu* calculation and fitting methods is conducted, based on the experimental data gathered.

2. Experimental facility

2.1. Airfoil-fin PCHE

An airfoil-fin PCHE, composed of 26 layers of cold-side heat exchange plates and 25 layers of hot-side heat exchange plates, was manufactured utilizing 316L stainless steel, and the thickness of each plate was 1.2 mm. Using photochemical etching techniques, all plates were arranged with identically sized NACA0025 airfoil fins in a staggered layout. These staggered airfoil fins constituted the channels, with each plate featuring 102 channels. To ensure the proper arrangement of the PCHE's headers, there are some differences between the cold and hot side plates. The inlet and outlet areas of the hot-side plates feature sections of L-shaped straight channels. Additionally, the inlet and outlet areas of the cold-side plates also have a small portion of straight channels to achieve a more uniform flow distribution, as presented in Fig. 1. The PCHE core dimension is 601.2 mm × 153 mm × 86 mm. Using a counterflow configuration, the heat transfer capacity can exceed 175 kW, making this airfoil-fin PCHE a viable solution for thermal systems.

Fig. 2 demonstrates the structure arrangement of the PCHE. As evident, the core of the NACA0025 airfoil-fin PCHE is formed by alternately stacking cold and hot-side plates. Each plate incorporates channels composed of airfoil fins (depicted in blue) and straight passages (depicted in green). Table 2 outlines the critical parameters of the airfoil-fin PCHE. The dimensions of the airfoil fin include a height (H_{fin}) of 0.8 mm, a width (W_{fin}) of 0.6 mm, a chord length (L_{fin}) of 2.4 mm, a top surface area (S_{top}) of 0.98 mm^2, and an end face perimeter (P_{fin}) of 5.1 mm. With a horizontal pitch (L_h) of 4.8 mm, a vertical pitch (L_v) of 1.2 mm, and a staggered pitch (L_s) of 2.4 mm, the airfoil fins are organized in a staggered pattern on the plate surface.

2.2. Experimental system

The current study set up a test rig to evaluate the thermal-hydraulic performance of the PCHE, as illustrated in Fig. 3. The experimental system mainly consisted of 4 parts: high-temperature water loop, supercritical pressure hydrocarbon fuel path system, cooling system, and data acquisition system. For the high-temperature water loop, water is driven by a circulating pump and regulated to a specific mass flow rate through a throttle valve. Subsequently, the water is heated by an electric heater before entering the PCHE for heat transfer. To prevent water from boiling, which could affect the stability of the system, nitrogen gas is first used to pressurize the water in the water storage tank before the experiment begins, thereby increasing the boiling point of water. Along the supercritical pressure hydrocarbon fuel path, room-temperature
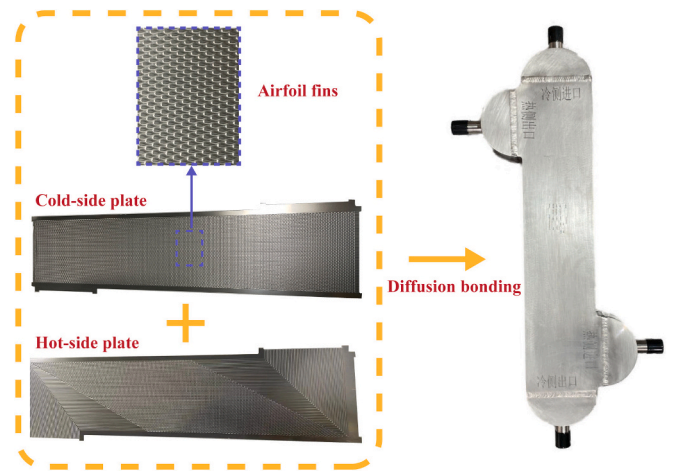

Fig. 1. Photos of the airfoil-fin PCHE.

Chinese hydrocarbon fuel RP-3 is driven by a fuel pump to flow into the PCHE and participate in heat exchange. Subsequently, the heated fuel undergoes cooling in a water cooler before passing through a back pressure valve to maintain optimal pressure levels within the fuel-path system. Finally, the fuel is returned to the RP-3 recycling tank. When the water-water heat transfer experiment of PCHE was conducted, the supercritical pressure hydrocarbon fuel path system was replaced with a water loop, similar to the high-temperature water loop except that there was no electric heater. As for the cooling system, using water as the cooling medium comprises components such as a water cooler, water pump, cooling water tower, and so on. In the experimental setup, the data acquisition system employs Coriolis mass flowmeters, ROSE-MOUNT pressure transmitters, and K-type sheathed thermocouples to collect data on fluid mass flow rates, inlet pressure and pressure drop, and inlet and outlet temperatures of the PCHE, respectively. The data acquisition process involves the utilization of several modules (ADAM 4118) to collect all measured data. These data are then integrated into the ADAM 4520, which serves as the central hub for signal aggregation before being connected to a data processing program within the computer. All test sections and pipelines within the experimental system are insulated with thermal insulation materials.

3. Data reduction and uncertainty analysis

3.1. Heat transfer data reduction

To assess the thermal-hydraulic performance of the airfoil-fin PCHE, the experimental data processing involves the utilization of the following formulas.

Defining an appropriate hydraulic diameter (d) for the airfoil-fin channel poses challenges. The definition provided in Ref. [16] has gained widespread acceptance for its applicability to airfoil-fin channels with various geometry parameters. The hydraulic diameter (d) can be determined using Eqs. (1)–(3) by defining an element.

$$V = \left(L_h L_v - S_{top}\right)H_{fin} \tag{1}$$

$$S = P_{fin}H_{fin} + 2\left(L_h - L_{fin}\right)H_{fin} + 2\left(L_h L_v - S_{top}\right) \tag{2}$$

$$d = \frac{4V}{S} \tag{3}$$

The heat transfer rates of the fuel side and water side are calculated using the measured temperatures, mass flow rates (m_{fuel}, m_{water}), and the isobaric specific heat capacity (c_p) of different working mediums at the average temperature ($T_{ave} = (T_{in} + T_{out})/2$), as below. The thermal properties of supercritical pressure hydrocarbon fuel RP-3 are obtained
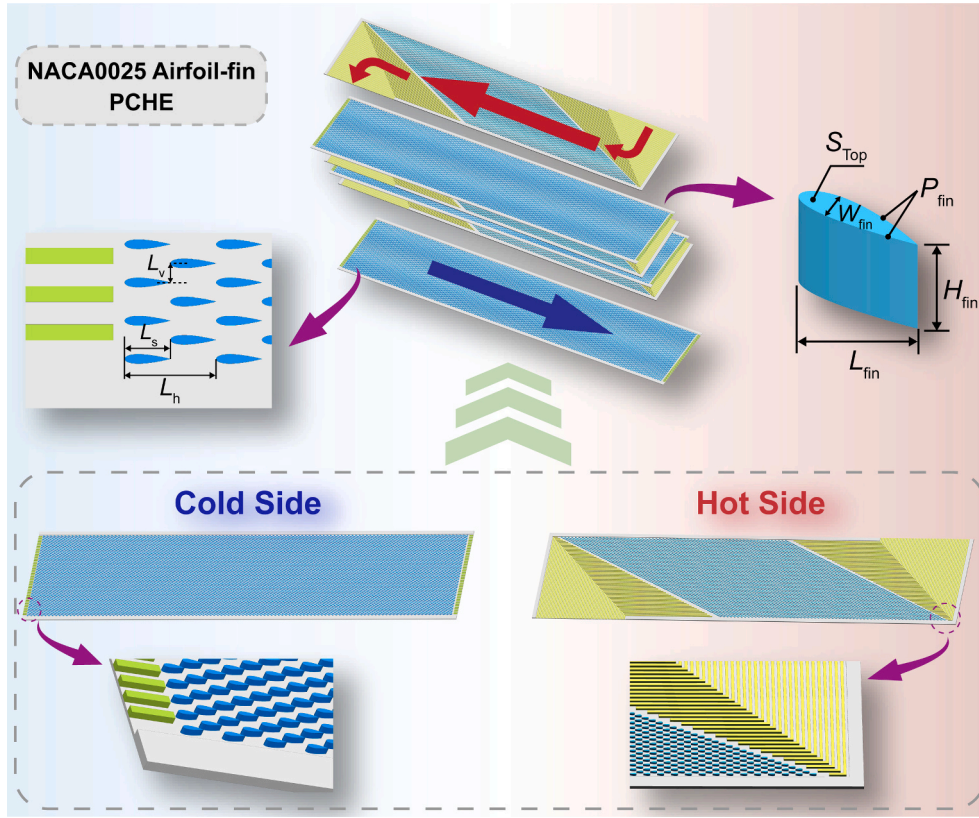
Fig. 2. Schematic diagram of the PCHE.

Table 2
Critical parameters of the airfoil-fin PCHE.

Parameters	Value	Parameters	Value
Plate length	601.2 mm	Plate width	153 mm
Plate thickness	1.2 mm	Height of fin, H_{fin}	0.8 mm
Width of fin, W_{fin}	0.6 mm	Chord length of fin, L_{fin}	2.4 mm
Top surface area, S_{top}	0.98 mm²	End face perimeter, P_{fin}	5.1 mm
Horizontal pitch, L_h	4.8 mm	Vertical pitch, L_v	1.2 mm
Staggered pitch, L_s	2.4 mm		

from the experimental measurements in the literature [45–48]. And the thermal properties of water at different pressures and temperatures are sourced from the open-source CoolProp database [49].

$$Q_{fuel} = m_{fuel}c_{p,fuel}\left(T_{c,out} - T_{c,in}\right) \tag{4}$$

$$Q_{water} = m_{water}c_{p,water}\left(T_{h,in} - T_{h,out}\right) \tag{5}$$

where subscriptions 'fuel', 'water', 'c', 'h', 'in', and 'out' represent the supercritical pressure hydrocarbon fuel RP-3, water, cold-side fluid, hot-side fluid, inlet, and outlet, respectively.

The heat transfer rate of the PCHE is defined as:

$$Q_{ave} = \frac{Q_{fuel} + Q_{water}}{2} \tag{6}$$

The overall heat transfer coefficient of the PCHE can be written as:

$$K = \frac{Q_{ave}}{\Delta T_m A} \tag{7}$$

where A is the heat transfer area, and ΔT_m is the logarithmic mean temperature difference, which is computed by the following equation.

$$\Delta T_m = \frac{\left(T_{h,in} - T_{c,out}\right) - \left(T_{h,out} - T_{c,in}\right)}{ln\left(\frac{T_{h,in} - T_{c,out}}{T_{h,out} - T_{c,in}}\right)} \tag{8}$$

Based on the analysis of thermal resistance, K can also be expressed as:

$$K = \frac{1}{\frac{A}{A_h}h_h + \frac{A\delta}{A_w\lambda_w} + \frac{A}{A_c}h_c} \tag{9}$$

where A_w, A_h, A_c is the heat transfer area of the wall, hot-side fluid, and cold-side fluid, respectively; h_h, h_c represent the HTC of the hot-side fluid, and cold-side fluid, respectively; λ_w is the thermal conductivity of the wall, which is 16.3 W/(m·K), and δ is the thickness of the bottom layer of the plate, with a value of 0.4 mm.

The thermal resistance of hot-side fluid, cold-side fluid, and wall is defined by the Eqs. (10)–(12).

$$R_h = \frac{1}{h_h A_h} \tag{10}$$

$$R_c = \frac{1}{h_c A_c} \tag{11}$$

$$R_w = \frac{\delta}{A_w \lambda_w} \tag{12}$$

The overall thermal resistance of the PCHE is given as:

$$R = \frac{1}{KA} = \frac{\Delta T_m}{Q_{ave}} = R_h + R_w + R_c = \frac{1}{h_h A_h} + \frac{\delta}{A_w \lambda_w} + \frac{1}{h_c A_c} \tag{13}$$

The Reynolds number, Prandtl number (*Pr*), and Nusselt number are defined as follows:

Fig. 3. Schematic diagram of the test rig for PCHE.

$$Re = \frac{4m}{\mu \pi d} \tag{14}$$

$$Pr = \frac{\mu c_p}{\lambda} \tag{15}$$

$$Nu = \frac{hd}{\lambda} \tag{16}$$

where m, μ, λ represents mass flow rate, dynamic viscosity, and thermal conductivity of the fluid, respectively. Assuming that the Nu correlations for the cold and hot fluids are both in the form of the Dittus-Boelter equation [50], expressed as follows:

$$Nu = CRe^a Pr^b \tag{17}$$

where C, a, and b are coefficients. Combined Eq. (10), (11), and (16), the thermal resistance of fluids can be rewritten as:

$$\begin{cases} R_h = \dfrac{d}{C_h Re_h^{a_h} Pr_h^{b_h} \lambda_h A_h} \\ R_c = \dfrac{d}{C_c Re_c^{a_c} Pr_c^{b_c} \lambda_c A_c} \end{cases} \tag{18}$$

By combining Eq. (13) and (18), the calculation equation for overall thermal resistance can be derived as shown in Eq. (19). It is evident that Eq. (19) involves six undetermined constants: C_h, a_h, b_h, C_c, a_c, and b_c.

$$R = \frac{\Delta T_m}{Q_{ave}} = \frac{d}{C_h Re_h^{a_h} Pr_h^{b_h} \lambda_h A_h} + R_w + \frac{d}{C_c Re_c^{a_c} Pr_c^{b_c} \lambda_c A_c} \tag{19}$$

3.2. Pressure drop data reduction

In the experiment, the measured pressure drop consists of the pressure drop across the PCHE core, the pressure drop caused by flow acceleration, and the pressure drop resulting from expansions and contractions at the PCHE headers, as shown in Eq. (20). However, only the pressure drop across the PCHE core is the focus of this study because it directly reflects the hydraulic characteristics of the airfoil-fin PCHE. The pressure drops in other parts can be considered as the minor losses. Therefore, following the reference [27, 37], this study calculates the minor loss pressure drop terms using minor loss coefficients, as follows.

$$\Delta P_{total} = \Delta P_{core} + \Delta P_{acceleration} + \Delta P_{in,expansion} + \Delta P_{in,contraction} + \Delta P_{out,expansion}$$
$$+ \Delta P_{out,contraction} \tag{20}$$

$$\Delta P_{acceleration} = (\rho u^2)_{out} - (\rho u^2)_{in} \tag{21}$$

$$\Delta P_{minor} = \sigma_{loss} \frac{\rho u^2}{2} \tag{22}$$

where u is the fluid velocity and σ_{loss} is the minor loss coefficient. The fluid velocity (u) can be calculated by Eq. (23), where A_c is the cross-sectional area. The value of σ_{loss} is determined by the geometric parameters of the PCHE. Based on Reference [51], the coefficients of other pressure drop terms are summarized in Table 3.

$$u = \frac{m}{\rho A_c} \tag{23}$$

The friction coefficient of the PCHE core is defined by the following equation.

$$f = \Delta P_{core} \frac{d}{L_{core}} \frac{1}{(1/2)\rho u^2} \tag{24}$$

where L_{core} represents the distance between the core inlet and core outlet.

3.3. Uncertainty analysis

Table 4 summarizes the uncertainty and working range of the direct measurements for the experimental facility. Based on the error propagation formula, for variables x_1, x_2, …, x_n, which are used in the

Table 3
Minor loss coefficient of the airfoil-fin PCHE.

Parameters	Value
Inlet header expansion	0.95
Inlet header contraction	0.45
Outlet header expansion	0.48
Outlet header contraction	0.17

computation of the variable (y) based on Eq. (25), given measurements with uncertainties δx_1, δx_2, ..., δx_n. If uncertainties in x_1, x_2, ..., x_n are independent and random, the uncertainty in y is:

$$y = f(x_1, x_2, ..., x_n) \tag{25}$$

$$\delta y = \sqrt{\left(\frac{\partial y}{\partial x_1}\delta x_1\right)^2 + \left(\frac{\partial y}{\partial x_2}\delta x_2\right)^2 + \cdots + \left(\frac{\partial y}{\partial x_n}\delta x_n\right)^2} \tag{26}$$

Combining the uncertainty of direct measurements, the calculated relative uncertainties of Re, K, and Q_{ave} are 2.29 %, 5.20 %, and 5.12 %, respectively. The detailed calculation process of uncertainty analysis can be referred to our past works [52,53], which have a similar experimental setup to this study.

4. Results and discussion

4.1. Experimental conditions and heat balance

To explore the thermal-hydraulic characteristics of airfoil-fin PCHE with supercritical pressure hydrocarbon fuel (RP-3) [54] or water as working mediums, the present study conducted experiments on both fuel-water and water-water heat exchange within the PCHE. In Fig. 4, the average temperature, Re, and inlet pressure of all experimental data points are presented for both the cold-side and hot-side fluids in the two sets of experiments using different working mediums. The detailed experimental conditions for fuel-water heat exchange are listed in Table 5. Besides, all experimental data is provided in the Appendix. To ensure the accuracy of the experimental data points, each data point was calculated as the average of at least four different time points measured within 20 s under stable operating conditions. The utilization of thermal insulation materials encompassing all tubes and the PCHE, coupled with the employment of water as the working medium possessing a high specific heat capacity, has substantially mitigated heat losses throughout the experimental procedure. Consequently, the influence of heat loss has been ignored in the data analysis. Furthermore, the maximum heat load among all test conditions is 41.57 kW. Since there is no existing research in the literature on the experimental study of thermodynamic performance of airfoil-fin PCHE using supercritical pressure hydrocarbon fuel as the working medium, in the subsequent discussion and analysis in this paper, the focus will primarily be on the results of the fuel-water heat exchange experiments.

Fig. 5 depicts the thermal properties variation of supercritical pressure hydrocarbon fuel (RP-3) and water with temperature and the orange shaded area represents the range of temperature variations of the working fluids observed during the experiments. The critical point of Chinese hydrocarbon fuel RP-3 is $T_{critical} = 645.04$ K, $P_{critical} = 2.33$ MPa [55]. It can be observed that only dynamic viscosity undergoes significant variations, while other thermal properties exhibit minor variations with temperature and mostly follow a linear trend.

The comparison of heat transfer rates between the hot and cold sides, as illustrated in Fig. 6, shows a relative deviation within 12 % between the two sides, indicating that the data obtained from the experiments are reliable. The process of heat transfer from the hot-side fluid to the cold-side fluid results in thermal losses. Therefore, during the experiment, the heat transfer rate of the hot-side fluid typically outweighs that of the cold-side fluid across all data points. Fig. 7 presents the overall HTC,

Table 4
Working range and uncertainty of direct measurements.

Direct measurement	Range	Uncertainty
Hot-side fluid mass flow rate	0–0.5 kg/s	±0.2 %
Cold-side fluid mass flow rate	0–2 kg/s	±0.2 %
Temperature	223.15–1423.15 K	±1.5 K
Absolute pressure	0–10 MPa	±0.04 %
Pressure drop	0–100 kPa	±0.04 %

calculated by Eq. (7), based on the cold-side heat transfer area (K_c) of experimental data as a function of Re_{water} and Re_{fuel}. The highest K_c value recorded is 719.2 W/(m²·K), observed at $Re_{fuel} = 198$ and $Re_{water} = 317$. For such extremely low Re of both hot and cold side fluids, the airfoil-fin PCHE still exhibits a high overall HTC, indicating its excellent heat transfer performance.

4.2. Flow characteristics and development of friction coefficient correlation

Fig. 8 illustrates the variation of the ratio of pressure drop across the PCHE core to the total measured pressure drop as a function of Re. In all experimental conditions, the ratio is greater than 0.92, indicating that the pressure drop in the PCHE is mainly due to the pressure drop across the PCHE core, while the pressure drop caused by the sudden expansion and contraction at the PCHE headers is relatively small. However, as Re increases, the pressure drop attributed to flow acceleration and the sudden expansion and contraction at the PCHE headers also increase.

To accurately predict the hydraulic performance of different working mediums inside the airfoil-fin PCHE, the present study utilized the Levenberg-Marquardt algorithm [56] based on experimental data to develop the friction coefficient correlation through least squares fitting. The form of friction coefficient correlation is the Blasius correlation form shown by Eq. (27). Fig. 9 presents the comparison of the proposed friction coefficient correlation of supercritical pressure fuel, as shown in Eq. (28), with the experimental data. The 95.2 % of the data fall within an ±8 % error band, indicating that the correlation predicts with good accuracy.

$$f = CRe^a \tag{27}$$

$$f_{fuel} = 10.6983Re_{fuel}^{-0.4548}, \quad 80 < Re_{fuel} < 246 \tag{28}$$

On the basis of the experiments on water-water heat exchange within the airfoil-fin PCHE, the current research also proposed the friction coefficient correlation of water, as presented in Eq. (29), in which the prediction errors between the proposed correlation and experimental data are within ±10 %.

$$f_{water} = 7.8933Re_{water}^{-0.3377}, \quad 50 < Re_{water} < 450 \tag{29}$$

The hydraulic performance of the airfoil-fin PCHE was compared with the straight PCHE and zigzag PCHE. As the friction coefficient only varies with Re, this study compares the correlation proposed by the experimental studies in Ref [19,57], which cover the Re range of the current study. It can be observed from Fig. 10 that, under laminar flow conditions, the airfoil-fin PCHE has the highest friction coefficient, while the one with straight fins has the lowest friction coefficient, and it is close to the one with zigzag fins. Within the Re range of 86 to 246, the average friction coefficient for the airfoil-fin PCHE is 2.93 times higher than that of the straight-channel PCHE, and 2.25 times higher than that of the zigzag PCHE.

The proposed friction coefficient correlation of fuel within airfoil-fin PCHE was also compared with other experimental research on airfoil-fin PCHEs, as shown in Fig. 11. Table 6 presents the f correlations derived from experimental investigation for comparative analysis. Although these studies focus on airfoil-fin PCHEs and feature similar channel shapes to current work, the structural parameters of the channels also have a significant impact on hydraulic characteristics. Due to the lack of hydraulic diameters for the channels in the references, the vertical pitch L_v (defined in Fig. 2) is used to represent the channel size. Observations indicate that the airfoil shape is beneficial for enhancing the hydraulic performance of PCHEs. Optimizing the airfoil-fin shape can significantly reduce the f. Additionally, the vertical pitch of the airfoil fins also has a significant impact on hydraulic performance, with a larger vertical pitch resulting in a smaller f.

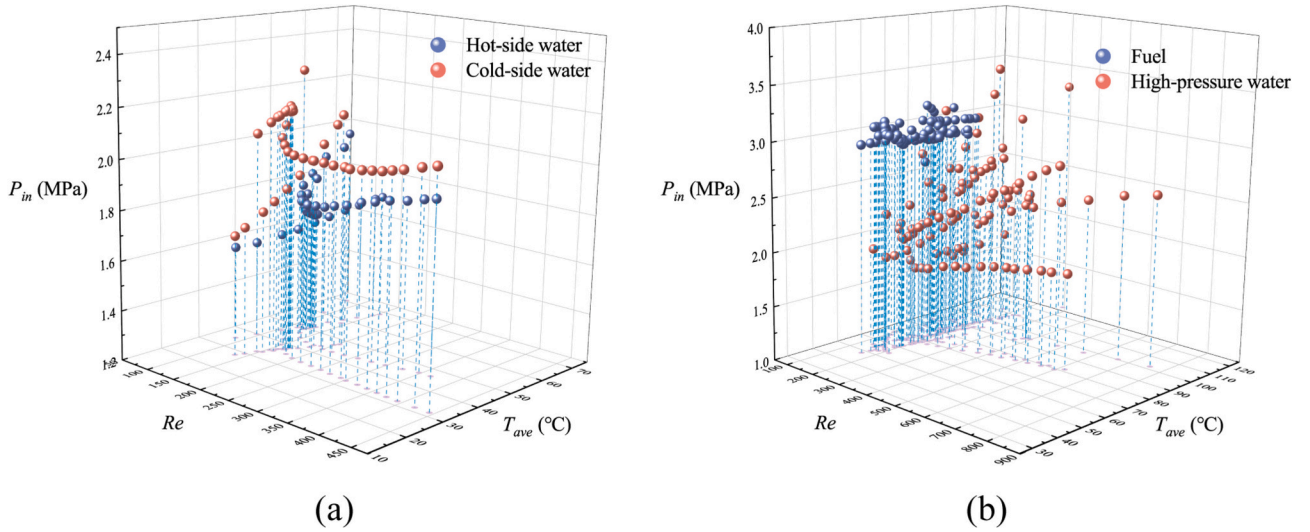The airfoil-fin PCHE designed in this study, in order to achieve an

Fig. 4. Experimental data points with temperature, *Re*, and inlet pressure; (a) water-water heat transfer, (b) fuel-water heat transfer.

Table 5
Experimental conditions for water-fuel heat exchange.

Parameters	Hot side (water)	Cold side (fuel)
Mass flow rate	53.1–375.1 g/s	82.0–275.0 g/s
Reynolds number	111.9–755.8	86.8–245.8
Inlet Pressure	1.65–3.51 MPa	2.70–3.17 MPa
Inlet temperature	74.18–173.01 °C	26.90–50.17 °C

extremely high heat transfer area-to-volume ratio, features tightly packed airfoil fins within the heat transfer plates. The vertical pitch of the airfoil fins is 1.2 mm, and the hydraulic diameter of the channels is only 0.87 mm, resulting in a high friction coefficient. This also explains why the friction coefficient of the airfoil-shaped PCHE in the current study, as shown in Fig. 10, is higher than that of the zigzag PCHE and the straight PCHE. Specifically, the airfoil-fin configuration influences the fluid dynamics in several key ways: i). Boundary layer interference. Proximity of airfoil fins induces boundary layer interference, disrupting layer development and stabilization, thus elevating flow resistance and *f*; ii). Vortex generation. Close airfoil fins may foster vortices at trailing edges under specific conditions, increasing *f* due to interactions between

these vortices and inter-fin flows; iii). Flow separation potential. Despite their aerodynamic design, airfoil shapes can cause flow separation at certain angles or conditions, particularly in compact spaces, with shape curvature and thickness exacerbating the issue; iv). Increased surface contact. Tightly packed airfoil fins expand the contact surface area per fluid volume, raising frictional resistance, especially when fin surfaces enhance viscous drag.

4.3. Heat transfer characteristics and development of Nu correlation

The heat transfer characteristics of airfoil-fin PCHE were investigated under different working fluids *Re* and heating power conditions. Fig. 12 displays the variation of fluids inlet and outlet temperatures under different cases, with water as the hot-side fluid and supercritical pressure hydrocarbon fuel as the cold-side fluid. In the case of the water mass flow rate remaining constant as shown in Fig. 12(a), the outlet temperatures of both the cold and hot fluids continuously decrease with the increase of Re_{fuel}. It is attributed to the fact that *K* rises with the increasing fluid *Re*. Besides, when the Re_{fuel} is less than 110, it can be observed that the cold-side fluid outlet temperature closely approaches the hot-side fluid inlet temperature. This phenomenon arises due to the
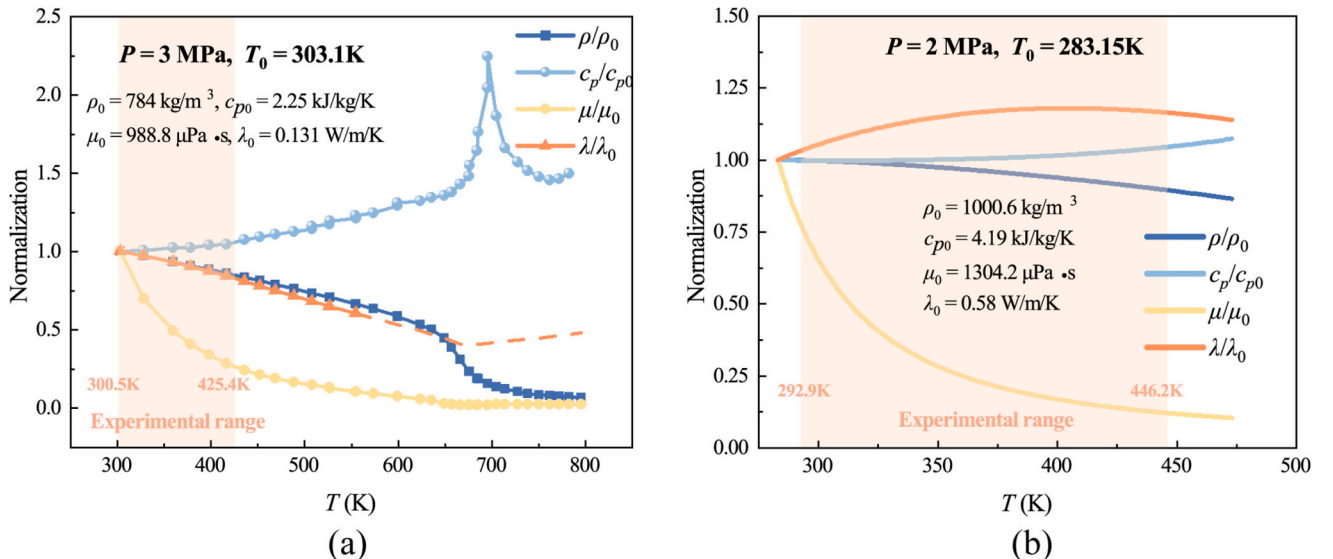

Fig. 5. Thermal properties variation of different working fluids with temperature; (a) supercritical pressure hydrocarbon fuel, (b) water.
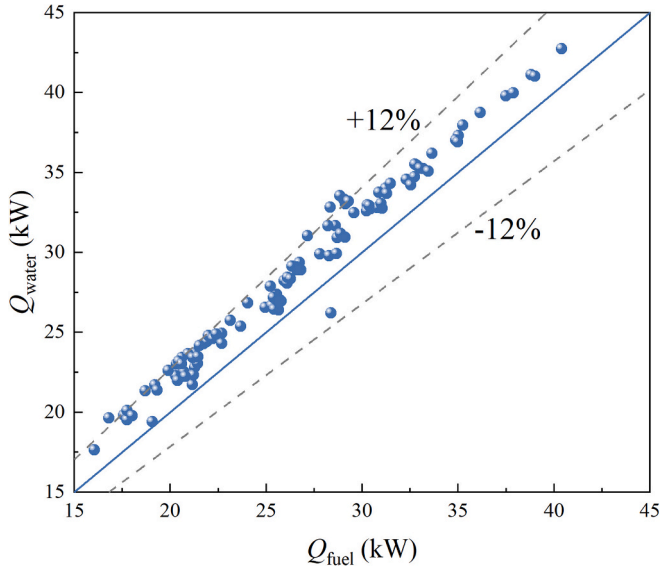
Fig. 6. Comparison of heat transfer rate between hot-side fluid and cold-side fluid.

relatively low mass flow rate of the cold-side fluid, coupled with the extensive heat exchange surface area of the PCHE, thereby approaching the heat transfer limit. The variation in the inlet temperature of the hot-side fluid is due to the closed-loop circulation of the hot-side fluid in the experimental system. Although the heating power remains constant, the outlet temperature of water from the PCHE changes under different operating conditions. Fig. 12(b) depicts the temperature variation in the situation where the fuel mass flow rate is kept constant and only the Re_{water} changes. A rise in Re_{water} leads to a progressive increase in the outlet temperature of the hot-side fluid, while the outlet temperature of the cold-side fluid remains relatively constant. This behavior is a consequence of the PCHE attaining its heat transfer limit at a relatively low Re_{water}. In other words, the outlet temperature of the cold-side fluid

approaches the inlet temperature of the hot-side fluid. Therefore, even as the Re_{water} increases, leading to an increase in the K, the outlet temperature of the cold-side fluid remains essentially unchanged. Regarding the effect of heating power on the inlet and outlet temperatures of the PCHE fluids, as the heating power increases, both the inlet and outlet temperatures of the PCHE rise as shown in Fig. 12(c), which aligns with conventional understanding.

The development of a Nu correlation specific to the airfoil-fin PCHE using experimental data is imperative to enhance the predictive accuracy of PCHE heat transfer performance within thermal systems. For fully-developed laminar flow in a straight pipe with uniform boundary conditions, the Nu remains unchanged, regardless of variations in the Re. Nevertheless, according to literature findings, the Nu for airfoil-fin channels or zigzag channels do not exhibit a constant value, even under laminar fully-developed flow conditions. In order to develop generalizable and accurate Nu correlations for fuel within the airfoil-fin
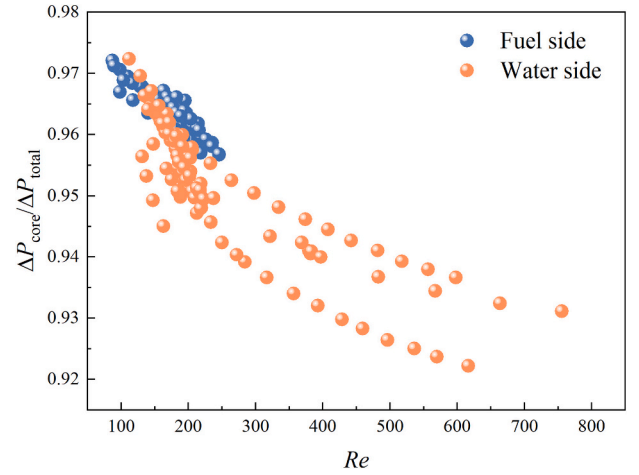

Fig. 8. The variation of the ratio of pressure drop across the PCHE core to the total measured pressure drop as a function of Re.
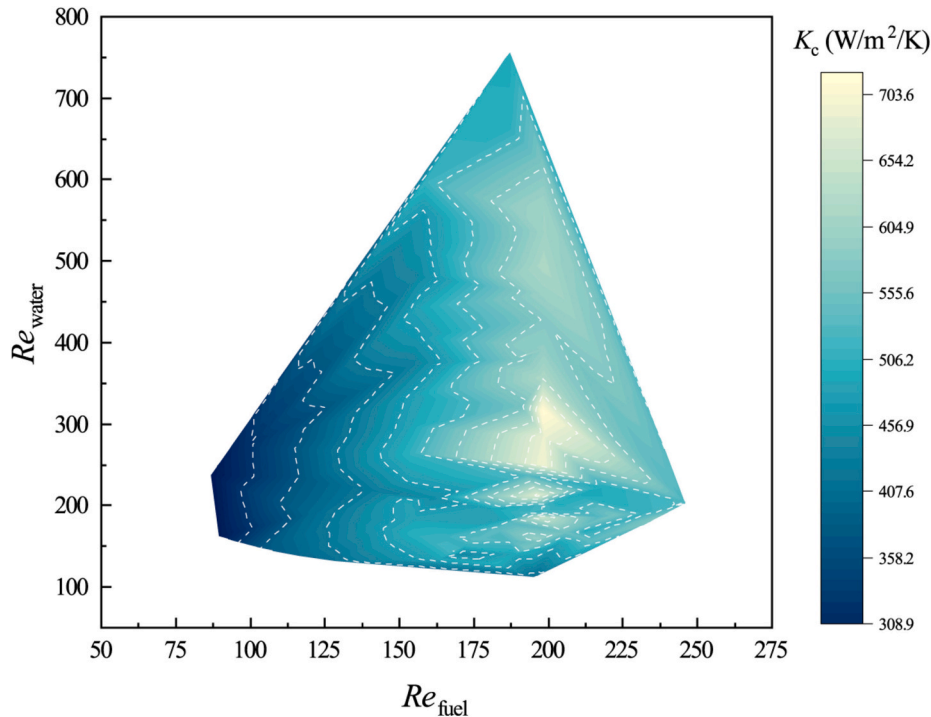

Fig. 7. Overall heat transfer coefficient based on the cold-side heat transfer area as a function of Re_{water} and Re_{fuel}.
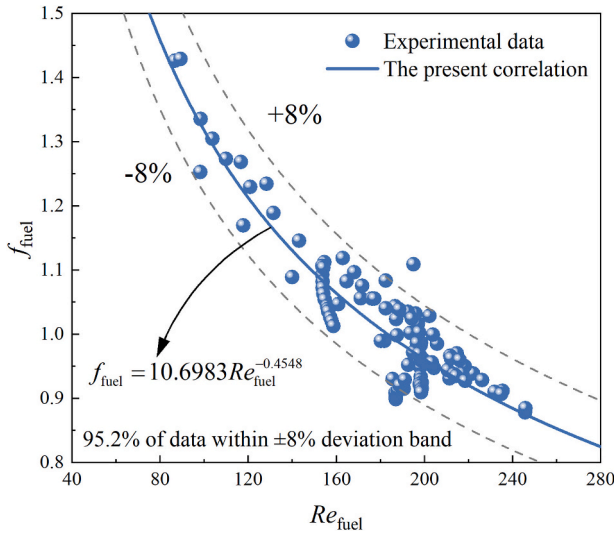
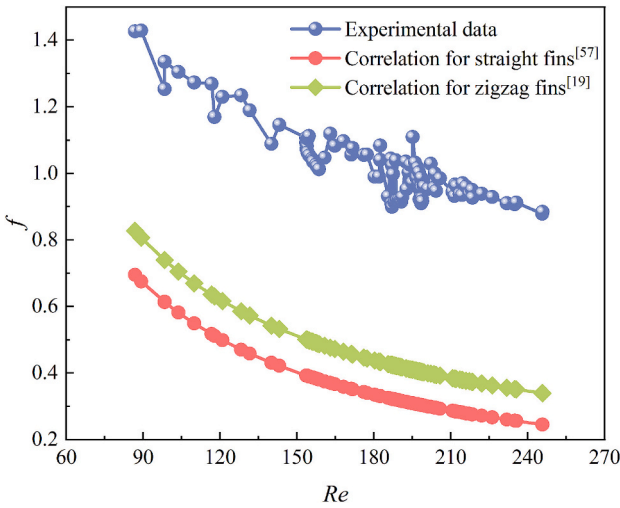**Fig. 9.** The variation of fuel friction coefficient with *Re*.

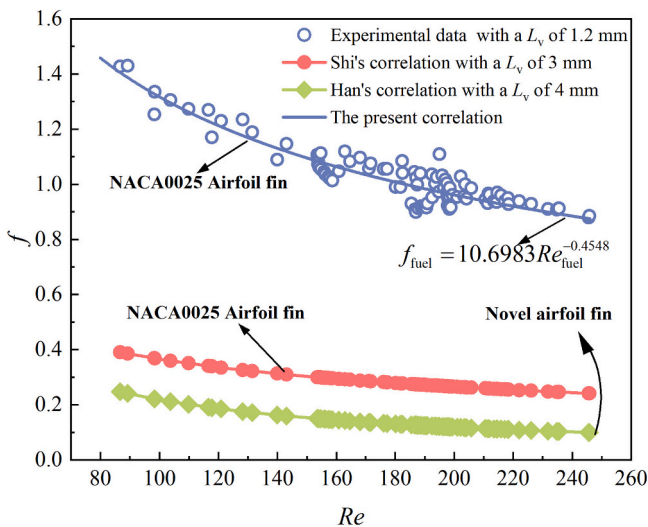**Fig. 10.** The comparison of PCHE friction coefficient with different fins.

Fig. 11. The comparison of airfoil-fin PCHE friction coefficient.

Table 6
The *f* correlations derived from experimental investigation for airfoil-fin PCHEs.

Reference	Airfoil shape	Vertical pitch (L_v)	Parameters range	Correlation
Shi et al. [42]	NACA0025	3 mm	$509 < Re < 6773$ $7.5 < Pr < 9.5$	$f = 3.07Re^{-0..462}$
Han et al. [43]	Novel airfoil	4 mm	$400 < Re < 2000$ $0.6 < Pr < 0.8$	$f = 12.3097Re^{-0.8755}$

PCHE, and to avoid the problem of infinite solution sets when solving the coefficients through nonlinear regression, this study adopted a method of conducting experiments with multiple sets of different working fluids. In other words, due to the similarity in structure between the cold and hot side plates, and the identical dimensions of the airfoil fins, it can be assumed that the heat transfer of the same working fluid flowing inside the cold and hot side plates follows the same *Nu* correlation. Although there are slight differences in the exponent of *Pr* in the *Nu* correlation when the working fluid is heated or cooled [58], its impact on the calculated Nusselt number is minor and within an acceptable margin of error. Besides, according to the literature findings, the exponent of *Pr* in the *Nu* correlation can be assumed to be 1/3. Therefore, for the same working fluid flowing inside the cold and hot side plates in the PCHE, there are only 2 undetermined coefficients (*C* and *a*) in Eq. (19) as shown by the following equation, so a unique real solution can be obtained through nonlinear regression fitting.

$$R = \frac{\Delta T_m}{Q_{ave}} = \frac{d}{CRe_h^a Pr_h^{1/3}\lambda_h A_h} + R_w + \frac{d}{CRe_c^a Pr_c^{1/3}\lambda_c A_c} \quad (30)$$

On the basis of the aforementioned analysis, the current study first carried out the water-water heat transfer experiments. Employing the Levenberg-Marquardt algorithm to perform nonlinear regression to determine the two unknown coefficients, the *Nu* correlation for water within the airfoil-fin PCHE was proposed by the following equation.

$$Nu_{water} = 0.000135Re_{water}^{1.8978}Pr_{water}^{1/3}, \; 112 < Re_{water} < 756, 1.35 < Pr_{water} < 5.10 \quad (31)$$

Subsequently, heat transfer experiments between supercritical pressure hydrocarbon fuel and water were conducted. By substituting Eq. (31) into Eq. (19), Eq. (32) is derived, which also consists of only two undetermined coefficients. Consequently, repeating the same nonlinear fitting process as before yielded the *Nu* correlation for supercritical pressure fuel within the airfoil-fin PCHE, as shown in Eq. (33). Fig. 13 illustrates the comparison of the proposed *Nu* correlation of fuel, as shown in Eq. (33), with the experimental data. The 86.7 % of the data fall within an ±20 % error band, indicating that the correlation predicts with good accuracy. Fig. 14 plots the comparison of the experimental overall thermal resistance of the PCHE with the calculated results using Eq. (31) and Eq. (33). The Nusselt number correlations proposed for water and supercritical pressure hydrocarbon fuel demonstrated the capability to predict the experimental overall thermal resistance of the airfoil-fin PCHE with a standard deviation of ±20 %. Notably, 93.3 % of the data fell within the ±20 % prediction margin, indicating a high level of prediction accuracy.

$$R = \frac{\Delta T_m}{Q_{ave}} = \frac{d}{0.000135Re_{water}^{1.8978}Pr_{water}^{1/3}\lambda_{water} A_h} + R_w + \frac{d}{CRe_{fuel}^a Pr_{fuel}^{1/3}\lambda_{fuel} A_c} \quad (32)$$

$$Nu_{fuel} = 0.07294Re_{fuel}^{0.6452}Pr_{fuel}^{1/3}, \; 80 < Re_{fuel} < 246, \; 8.3 < Pr_{fuel} < 10.7 \quad (33)$$

The heat transfer characteristics of the airfoil-fin PCHE in the

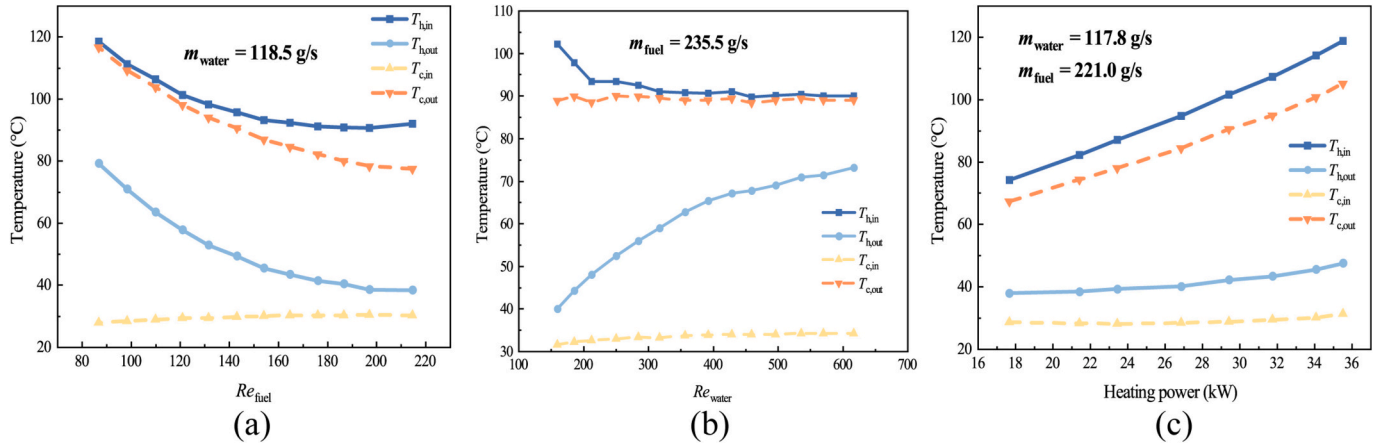**Fig. 12.** Fluids inlet and outlet temperature variation under different cases; (a) under varying Re_{fuel}, (b) under varying Re_{water}, (c) under varying heating power.

laminar regime were compared with the straight-fin PCHE, zigzag-fin PCHE, and S-shape PCHE. Due to the limited use of supercritical pressure hydrocarbon fuels in previous experimental studies on PCHE heat transfer, and considering that heat transfer correlations are closely related to the thermal properties of the working fluid, this study compared the Nu correlations proposed in this work for water (Eq. (31)) within the airfoil-fin PCHE with those obtained for different PCHE channel structures using water as th working fluid. Table 7 presents the Nu correlations derived from experimental investigation for comparative analysis, encompassing the Re and Pr ranges of this study. Fig. 15 depicts the comparison results between the experimental data for airfoil-fin PCHE and the existing correlations for other PCHE channel structures. It indicates that the superiority of the heat transfer performance of the airfoil-fin PCHE compared to other flow channel structures varies with the change in the working fluid flow Reynolds number. In laminar flow conditions, when $Re > 334$, the airfoil-fin PCHE exhibits the best heat transfer performance. Specifically, within the Re range of 334 to 756, the average Nu for the airfoil-fin PCHE is 7.74 times higher than that of the straight-channel PCHE, 3.15 times higher than that of the zigzag PCHE, and 1.65 times higher than that of the S-shaped PCHE. However, as Re decreases, the heat transfer performance of the airfoil-fin PCHE weakens. When $Re < 147$, its heat transfer performance may even be inferior to that of the straight-channel PCHE. In contrast, the heat
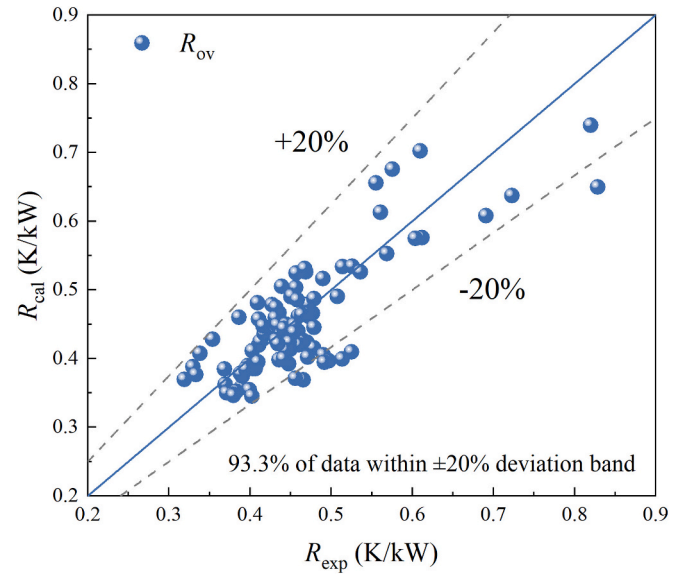

Fig. 14. The comparison of overall thermal resistance of PCHE (Calculated results vs Experimental data).
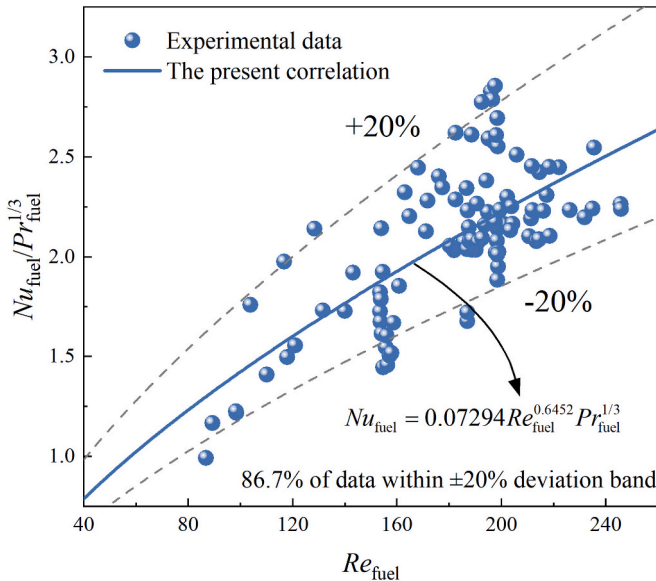
transfer performance of the S-shape, zigzag, and straight-channel PCHEs remains relatively stable. Notably, the S-shaped PCHE consistently outperforms the zigzag PCHE, which in turn is always superior to the straight-channel PCHE.

The proposed Nu correlation of fuel within airfoil-fin PCHE was also compared with other experimental research on airfoil-fin PCHEs, as shown in Fig. 16. Table 8 presents the Nu correlations derived from experimental investigation for comparative analysis. It can be observed

Fig. 13. The variation of fuel Nusselt number with Re.

Table 7

The Nu correlations derived from experimental investigation for different fins.

Reference	Channel shape	Parameters range	Correlation
Seo et al. [16]	Straight	$100 < Re < 850$ $3.5 < Pr < 5.2$	$Nu = 0.7203Re^{0.1775}Pr^{1/3}(\mu/\mu_w)^{0.14}$
Kim et al. [19]	Zigzag	$0 < Re < 2500$ $0.66 < Pr < 13.41$	$Nu = 4.089 + 0.00365Re^{1.00}Pr^{0.58}$
Tsuzuki et al. [59]	S-shape	$100 < Re < 1500$ $2 < Pr < 11$	$Nu = 0.253Re^{0.597}Pr^{0.349}$

that since both the PCHE in this study and those in the comparative literature use the NACA0025 airfoil shape and operate under similarly low *Re* conditions for the working fluid, the experimental data from this work are closely aligned with those, which further affirmed the reliability of the proposed correlation in this work. However, due to significant differences in the physical properties of the working fluids studied and variations in the channel structural dimensions, the calculated results of the *Nu* correlations derived from different airfoil-fin PCHE experimental studies also show noticeable differences.

4.4. Comparison of comprehensive thermal-hydraulic performance

On the basis of the aforementioned results, the airfoil-fin PCHE under laminar flow conditions exhibits a higher friction coefficient but superior heat transfer performance at high Reynolds numbers compared to other PCHE structures. Therefore, analyzing the comprehensive thermal-hydraulic performance of the airfoil-fin PCHE, which involves simultaneous consideration of heat transfer and pressure drop characteristics, is essential. The present study employs the performance evaluation criteria (PEC) to evaluate the comprehensive performance of different PCHE channels, which has been extensively used in lots of studies [24,25,27]. PEC is defined as follows:

$$\text{PEC} = \left(\frac{Nu}{Nu_{\text{ref}}}\right) \bigg/ \left(\frac{f}{f_{\text{ref}}}\right)^{1/3} \tag{34}$$

where *f* and *Nu* are obtained from friction coefficient correlations and *Nu* correlations specific to different channel structures, with the subscript "ref" representing the thermodynamic performance of straight PCHE in this study. A PEC value greater than one indicates superior overall thermal-hydraulic performance in the PCHE channel type compared to the straight PCHE.

Following a detailed literature review, it was found that thermal-hydraulic correlations for supercritical pressure hydrocarbon fuel in different structured PCHEs are lacking. Consequently, this study utilizes correlations derived from experiments using water as the working fluid to conduct a comparative analysis of the comprehensive performance of PCHEs. However, under laminar conditions, the friction correlation for water flowing in S-shaped PCHEs is lacking, rendering the calculation of the PEC for S-shaped PCHEs under laminar conditions unfeasible. Given these limitations, the work evaluates the comprehensive thermodynamic performance of straight-channel, zigzag, and airfoil-fin PCHEs, all using water as the working fluid under laminar conditions. Table 9
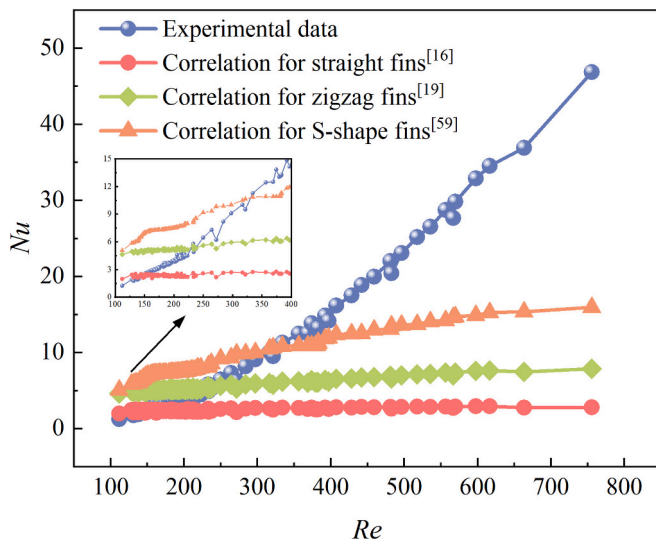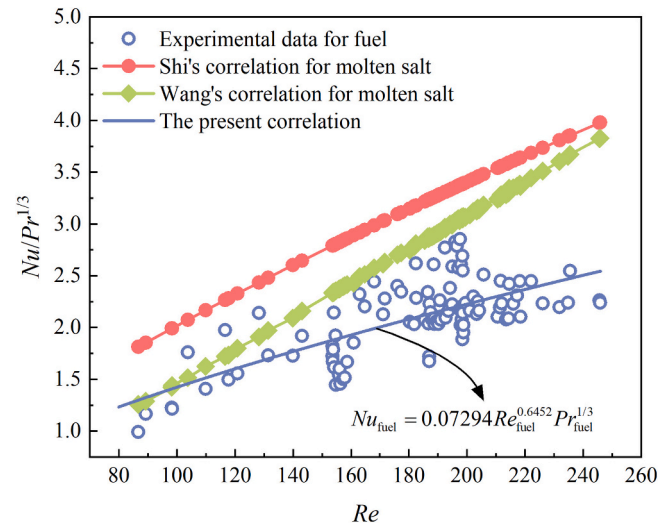

Fig. 16. The comparison of *Nu* of airfoil-fin PCHE.

presents the *Nu* correlations and *f* correlations derived from experimental investigation for comparative analysis, encompassing the *Re* and *Pr* ranges of this study.

Fig. 17 depicts the comparison results of PEC as a function of *Re* for various PCHE channel structures. The results indicate that the comprehensive thermodynamic performance of the airfoil-fin PCHE improves with increasing *Re*. Although the airfoil-fin PCHE designed in this study has a higher friction coefficient, when *Re* exceeds 265, the PEC of the airfoil-fin PCHE surpasses that of other channel-structured PCHEs. Within the *Re* range of 265 to 756, the average PEC of the airfoil-fin PCHE is 5.43 times higher than that of the straight-channel PCHE and 2.14 times higher than that of the zigzag PCHE. It is important to note that when the *Re* falls below 167, the comprehensive performance of the airfoil-fin PCHE is inferior to that of the straight-channel PCHE. This suggests that using an airfoil channel structure may not be a reasonable option under extremely low *Re* conditions. Additionally, under laminar flow conditions, the PEC for the zigzag PCHE remains relatively stable and consistently larger than that of the straight-channel PCHE. This indicates that the overall performance of the zigzag PCHE is superior to that of the straight-channel PCHE in the laminar regime.

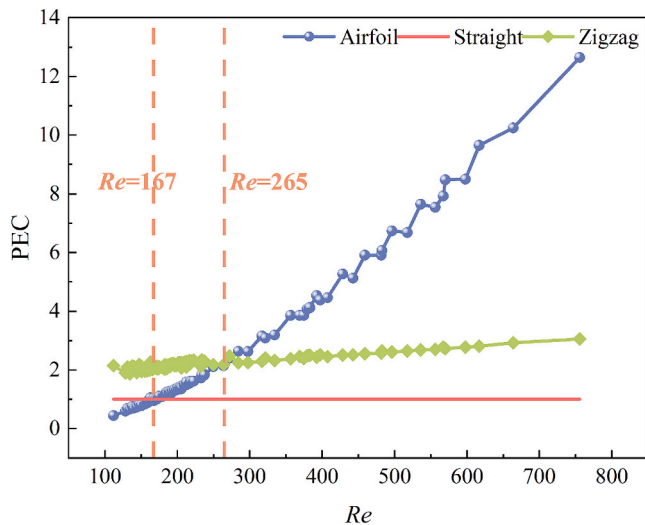### 4.5. Comparison of Nu calculation and fitting methods

Based on the analysis in the Introduction section, the Nusselt number obtained from different fitting algorithms for the cold and hot side fluids within the airfoil-fin PCHE may not represent their actual Nusselt number, potentially leading to significant deviations when applying the *Nu* correlation of a single fluid to the design of other PCHEs. Therefore, assessing the feasibility and applicability of *Nu* calculation and fitting methods in PCHE experimental studies is of more importance. Reviewing the existing experimental research listed in Table 1, the present work summarizes six commonly used methods for calculating and fitting *Nu* for the PCHE with different working fluids on the hot and cold sides, as indicated by Table 10. The present method has been described in Section 4.3. Method A uses the GA to compute all unknown coefficients in the *Nu* correlations for both hot-side fluid and cold-side fluid. Method B employs a constrained nonlinear multi-variable function solver based on the interior-point search algorithm to compute all unknown coefficients in the *Nu* correlations for both hot-side fluid and cold-side fluid. As for Method C and Method D, both of them obtain the *Nu* correlation of the cold-side or hot-side fluid through existing literature results and then perform nonlinear regression to solve for the *Nu* correlation of the other side fluid. Method E utilizes the modified Wilson plot method and the exponent for velocity is set to 0.8 to solve the *Nu* correlation of the

Fig. 15. The comparison of PCHE Nusselt number with different fins.

Table 8

The *Nu* correlations derived from experimental investigation for airfoil-fin PCHEs.

Reference	Airfoil shape	Working fluid	Parameters range	Correlation
Shi et al. [42]	NACA0025	Molten salt	$509 < Re < 6773$ $7.5 < Pr < 9.5$	$Nu = 0.063Re^{0.755}Pr^{1/3}(\mu/\mu_w)^{0.14}$
Wang et al. [41]	NACA0025	Molten salt	$500 < Re < 1548$ $19.4 < Pr < 23.8$	$Nu = 0.0090Re^{1.0731}Pr^{0.4}$

Table 9

Summary of *Nu* correlations and *f* correlations of different PCHE channel types for performance comparison.

Reference	Channel shape	Parameters range	Correlation
Seo et al. [16]	Straight	$100 < Re < 850$ $3.5 < Pr < 5.2$	$Nu = 0.7203Re^{0.1775}Pr^{1/3}(\mu/\mu_w)^{0.14}$ $f = 4 \times 1.3383Re^{-0.5003}$
Kim et al. [19]	Zigzag	$0 < Re < 2500$ $0.66 < Pr < 13.41$	$Nu = 4.089 + 0.00365Re^{1.00}Pr^{0.58}$ $f = 4 \times (15.78/Re + 0.0557Re^{-0.18})$
The present study	Airfoil	$112 < Re < 756$ $1.35 < Pr < 5.10$	Eq. (29) and Eq. (31)

Fig. 17. The comparison of the comprehensive thermal-hydraulic performance of various PCHE channels.

target-side fluid.

To evaluate the *Nu* calculation and fitting performance of the various methods illustrated in Table 10, the current study utilized experimental data on heat exchange between supercritical pressure hydrocarbon fuel and water in the airfoil-fin PCHE. Different methods were employed to calculate the *Nu* and fit the *Nu* correlation. Subsequently, their results were compared accordingly. In the calculation process, for Method C, the heat transfer correlation proposed by Shi et al. [42] is employed for the fuel side. The Shi correlation was developed for molten salt, with characteristics similar to the fuel utilized in this study. As for Method D, the Nusselt number of water side was computed by the Hausen equation [44], which was utilized for predicting the Nusselt number of fluids within the tube under the laminar regime. Fig. 18 illustrates the comparison of the calculated overall heat transfer coefficient of airfoil-fin PCHE with the experimental results using different *Nu* calculation methods. Except for Method D, the data from other methods generally fall within a deviation band of ±20 %. This suggests that the *Nu*

Table 10

Commonly used *Nu* calculation and fitting methods.

No.	Description
The present method	First, conducting experiments using the same working fluid on both sides. Subsequently, conducting experiments again using different working fluids on both sides. The *Nu* correlation is obtained through nonlinear regression fitting based on experimental data.
Method A	Using the GA to compute all unknown coefficients in the *Nu* correlations for both hot-side fluid and cold-side fluid.
Method B	Using a constrained nonlinear multi-variable function solver based on the interior-point search algorithm to compute all unknown coefficients in the *Nu* correlations for both hot-side fluid and cold-side fluid.
Method C	The *Nu* correlation for the cold-side fluid is determined using existing literature results, while a nonlinear regression fitting is employed to solve for the *Nu* correlation for the hot-side fluid.
Method D	The *Nu* correlation for the hot-side fluid is determined using existing literature results, while a nonlinear regression fitting is employed to solve for the *Nu* correlation for the cold-side fluid.
Method E	Using the modified Wilson plot method and the exponent for velocity is set to 0.8 to solve the *Nu* correlation of the target-side fluid.

correlations utilized for both the cold and hot side fluids obtained by these methods demonstrate a satisfactory level of accuracy in predicting the *K* of the airfoil-fin PCHE. Moreover, considering the significant predictive error associated with Method D, the Hausen equation is not suitable for calculating the Nusselt number of water flowing in the airfoil channels in the laminar regime.

However, the components of *K* calculation, namely the Nusselt numbers of the cold and hot side fluids calculated by different methods, exhibit significant deviations from each other. Table 11 summarizes the heat transfer correlations of the fuel side and water side within the airfoil-fin PCHE obtained from different methods. The variation of fuel *Nu* with *Re* for different methods was illustrated in Fig. 19. The present method and Method E demonstrated satisfactory predictive performance for the *Nu* of the fuel, closely matching experimental data. However, Methods A, B, and C exhibited overestimations in their predictions. Method B, in particular, showed a significant overestimation of the *Nu* for the fuel within the airfoil-fin PCHE, with *Nu* increasing exponentially with *Re*. As for Method D, the decrease in the fuel *Nu* with increasing *Re* contradicted the expected trend, which explained the significant deviation observed in the predicted *K* from Method D in Fig. 18. Fig. 20 showed the variation of water *Nu* with *Re* for different methods. The presented method still exhibited excellent predictive accuracy, and Method E demonstrated acceptable prediction performance within the range of $400 < Re < 550$, falling within the acceptable error range. However, Method E's predictive accuracy was poor in other *Re* ranges. Contrary to the predictive performance depicted in Fig. 19, Methods A, B, and C currently showed significant underestimation of the *Nu* for the water within the airfoil-fin PCHE. This outcome aligns with the expectation based on Eq. (9). When there is an overestimation of the HTC of the cold-side fluid (fuel), minimal prediction error in the *K* of the PCHE occurs only if there is a corresponding underestimation of the HTC of the hot-side fluid (water).

The *Nu* fitting deviation is defined as the absolute difference between the experimental *Nu* and the fitted *Nu*, divided by the experimental *Nu*, as shown in Eq. (35). And the average fitting deviation is the mean value
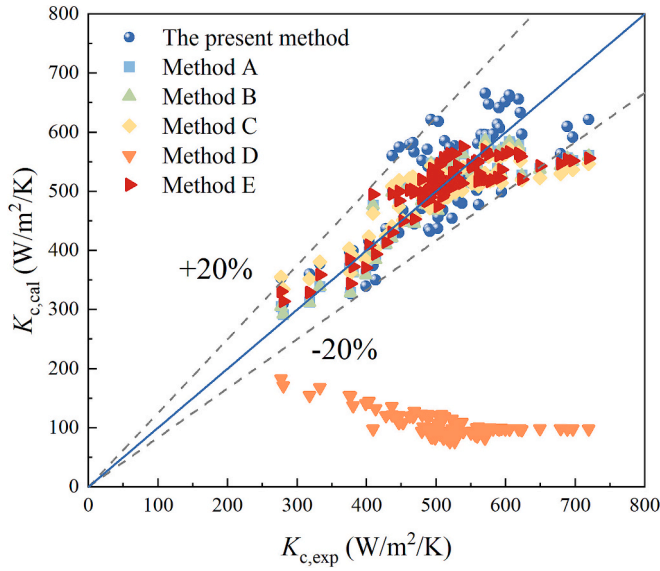
Fig. 18. The comparison of the overall heat transfer coefficient of airfoil-fin PCHE (Calculated results vs Experimental data).

Table 11
The heat transfer correlations obtained from different methods.

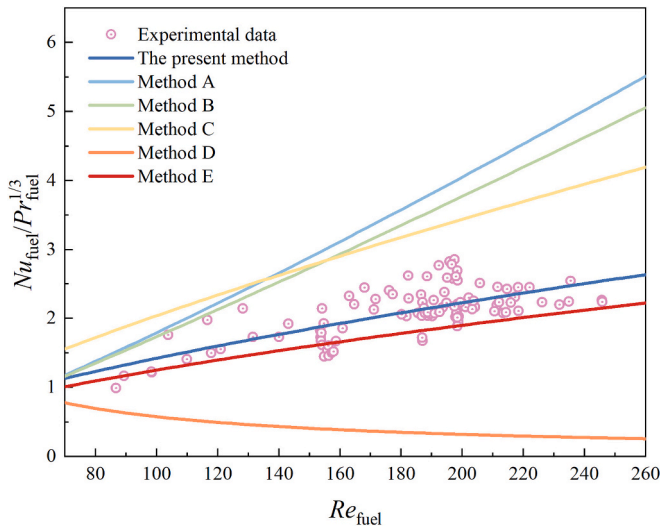| No.	Fuel side	Water side
The present method	$Nu = 0.07294Re^{0.6452}Pr^{1/3}$	$Nu = 0.000135Re^{1.8978}Pr^{1/3}$
Method A	$Nu = 0.008Re^{1.1753}Pr^{1/3}$	$Nu = 0.4571Re^{0.1615}Pr^{1/3}$
Method B	$Nu = 0.0153Re^{1.1197}Pr^{1/3}$	$Nu = 0.4582Re^{0.1712}Pr^{1/3}$
Method C	$Nu = 0.063Re^{0.755}Pr^{1/3}(\mu/\mu_w)^{0.14}$	$Nu = 0.4091Re^{0.198}Pr^{1/3}$
Method D	$Nu = 28Re^{-0.84302}Pr^{1/3}$	$Nu = 3.66 + \dfrac{0.0668(d/L)RePr}{1 + 0.04[(d/L)RePr]^{2/3}}$
Method E	$Nu = 0.0784Re^{0.60166}Pr^{1/3}$	$h = 59171.6u^{0.8}$

Fig. 19. The variation of fuel Nu with Re for different Nu calculation methods.

of all experimental data's fitting deviations, which is calculated by the Eq. (36). Fig. 21 plotted the average Nu fitting deviation for different methods. It can be observed that Methods A-E all exhibited significant fitting deviations. Such a degree of error is unacceptable for the high-precision design of airfoil-fin PCHE in thermal systems, as it can lead
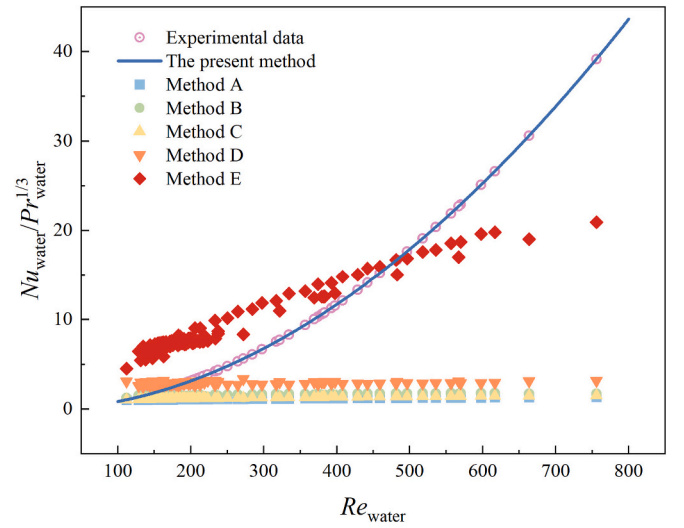

Fig. 20. The variation of water Nu with Re for different Nu calculation methods.

to substantial deviations in the design of heat transfer areas and cost issues, among other concerns. In other words, applying the Nu correlations obtained by these methods to the design of other PCHEs may result in significant design deviations. Currently, the relatively feasible approach appears to be utilizing the present method, of which the average fitting deviation is below 10 %. That is, first, conducting experiments using the same working fluid on both sides. Subsequently, conducting experiments again using different working fluids on both sides. The Nu correlation is obtained by employing the Levenberg-Marquardt algorithm to perform nonlinear regression based on experimental data.

$$\varepsilon = \left| \frac{Nu_{\exp} - Nu_{\text{cal}}}{Nu_{\exp}} \times 100\% \right| \tag{35}$$

$$\varepsilon_{\text{ave}} = \left(\sum_{i=1}^{n} \varepsilon_i \right) / n \tag{36}$$

5. Conclusion

This study established an experimental platform to systematically investigate the thermal-hydraulic performance of the PCHE with NACA0025 airfoil fins. The heat transfer and pressure drop correlations for supercritical pressure hydrocarbon fuel and water flowing in the airfoil-fin PCHE were developed, with a standard deviation of ± 8 % for f and ± 20 % for Nu. The thermodynamic performance of the airfoil-fin PCHE was compared with that of straight, zigzag, and S-shaped PCHEs. Additionally, a comparative assessment of six different Nu calculation and fitting methods from existing literature was conducted to address challenges associated with improper analysis of heat transfer characteristics and its impact on the high-precision design of PCHEs. These methods include GA, global optimization algorithms based on the interior point method, known Nu correlations for the cold-side fluid, known Nu correlations for the hot-side fluid, and the modified Wilson plot method. The current findings contribute to a deeper understanding of the thermal-hydraulic performance of airfoil-fin PCHE under laminar regime and provide quantitative analysis and appropriate methods for the Nu calculation in PCHE experimental studies. The remarkable findings of this investigation can be summed up as follows.

   i. The hydraulic performance of the airfoil-fin PCHE was compared with the straight-channel PCHE and zigzag PCHE. Under laminar flow conditions, the airfoil-fin PCHE has the highest f, while the
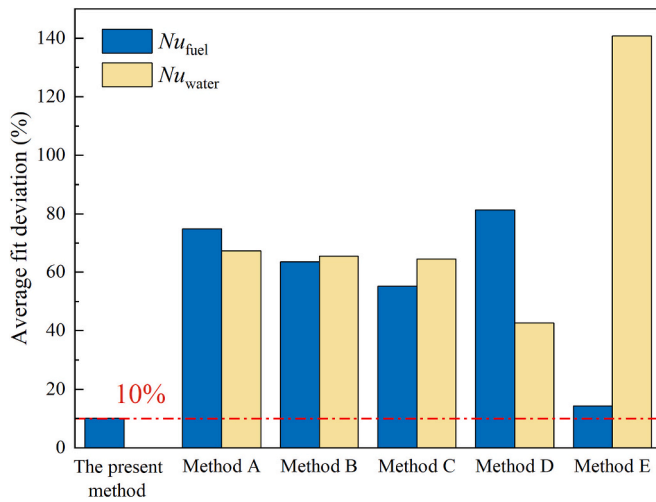
Fig. 21. The average *Nu* fitting deviation for different methods.

higher than that of the zigzag PCHE. This indicates that, under conditions of laminar flow and higher *Re*, the airfoil channel configuration is likely the most effective.

iv. Six methods commonly used for calculating and fitting *Nu* for PCHEs with different working fluids on both the hot and cold sides were assessed. Results reveal significant fitting deviations for Methods A-E, making them unsuitable for the high-precision design of airfoil-fin PCHEs. The relatively feasible approach appears to be utilizing the present method, i.e., conducting experiments with multiple sets of different working fluids, which has an average fitting deviation of less than 10 %.

Declaration of generative AI and AI-assisted technologies in the writing process

During the preparation of this work the author(s) used Youdao AIBox and ChatGPT in order to check grammar and improve readability. The author(s) did not use this tool/service to directly generate the manuscript but only to polish the manuscript written by the author(s). After using this tool/service, the author(s) reviewed and edited the content as needed and take(s) full responsibility for the content of the publication.

CRediT authorship contribution statement

Weitong Liu: Writing – original draft, Software, Investigation, Formal analysis, Data curation. **Guoqiang Xu:** Project administration, Conceptualization. **Haoxing Zhi:** Resources. **Ruoyu Wang:** Resources. **Mowen Li:** Validation. **Yanchen Fu:** Writing – review & editing, Supervision, Methodology, Funding acquisition.

Declaration of competing interest

The authors declare that they have no known competing financial interests or personal relationships that could have appeared to influence the work reported in this paper.

Acknowledgment

one with straight fins has the lowest *f* coefficient, and it is close to the one with zigzag fins. Within the *Re* range of 86 to 246, the average *f* for the airfoil-fin PCHE is 2.93 times higher than that of the straight-channel PCHE, and 2.25 times higher than that of the zigzag PCHE.

ii. The heat transfer performance of the airfoil-fin PCHE in laminar flow was compared with straight, zigzag, and S-shape PCHEs. The superiority of the airfoil-fin PCHE compared to other channel types depends on *Re*. For *Re* > 334, the airfoil-fin PCHE shows the best heat transfer performance. In the *Re* range of 334 to 756, the airfoil-fin PCHE exhibits an average *Nu* that is 7.74 times higher than the straight-channel PCHE, 3.15 times higher than the zigzag PCHE, and 1.65 times higher than the S-shaped PCHE. However, as *Re* decreases, its performance weakens. When *Re* < 147, it performs worse than the straight PCHE.

iii. The comprehensive performance of PCHEs with straight, zigzag, and airfoil fins was evaluated using the PEC. Results indicate that the comprehensive thermodynamic performance of the airfoil-fin PCHE improves with increasing *Re*. Notably, when *Re* exceeds 265, the PEC of the airfoil-fin PCHE surpasses that of other channel-structured PCHEs. Specifically, within the *Re* range of 265 to 756, the average PEC of the airfoil-fin PCHE is 5.43 times higher than that of the straight-channel PCHE and 2.14 times

Appendix A. Experimental data

This appendix gives the experimental data for the various cases.

A.1. Experimental data fuel-water heat transfer

Case No.	m_{fuel} (kg/s)	m_{water} (kg/s)	$T_{c,in}$ (°C)	$T_{c,out}$ (°C)	$T_{h,in}$ (°C)	$T_{h,out}$ (°C)	$P_{fuel,in}$ (MPa)	$\Delta P_{core,fuel}$ (kPa)	$P_{water,in}$ (MPa)	$\Delta P_{core,water}$ (kPa)	Q_{fuel} (kW)	Q_{water} (kW)	Q_{ave} (kW)
1	0.1937	0.0913	43.66	88.83	102.19	50.30	2.92	7.08	2.74	1.26	17.57	19.84	18.70
2	0.1931	0.1109	50.17	94.99	102.55	60.52	2.70	6.64	3.15	1.55	17.74	19.53	18.64
3	0.1960	0.1345	26.90	83.17	88.21	46.10	3.08	7.54	2.09	2.27	21.25	23.71	22.48
4	0.1957	0.1510	27.10	81.90	85.85	48.78	3.08	7.47	2.12	2.67	20.62	23.42	22.02
5	0.1960	0.1690	27.38	81.34	84.45	51.92	3.08	7.40	2.18	3.15	20.33	23.01	21.67
6	0.1958	0.1890	27.45	81.70	83.86	54.54	3.08	7.32	2.24	3.69	20.44	23.19	21.81
7	0.1959	0.2092	27.57	81.40	83.17	57.71	3.08	7.26	2.30	4.31	20.28	22.29	21.29
8	0.1960	0.2308	27.67	81.70	83.20	60.43	3.08	7.21	2.35	4.99	20.38	22.00	21.19
9	0.1958	0.2517	27.77	82.63	84.48	63.10	3.07	7.13	2.44	5.70	20.72	22.54	21.63
10	0.1960	0.2691	27.85	83.70	84.86	65.58	3.08	7.08	2.52	6.31	21.16	21.73	21.44
11	0.1958	0.2899	27.97	84.10	85.15	66.37	3.07	7.04	2.57	7.07	21.27	22.80	22.04
12	0.1955	0.3103	28.03	84.62	85.96	68.22	3.07	6.99	2.65	7.86	21.43	23.06	22.24

(continued on next page)

(continued)

Case No.	m_{fuel} (kg/s)	m_{water} (kg/s)	$T_{c,in}$ (°C)	$T_{c,out}$ (°C)	$T_{h,in}$ (°C)	$T_{h,out}$ (°C)	$P_{fuel,in}$ (MPa)	$\Delta P_{core,fuel}$ (kPa)	$P_{water,in}$ (MPa)	$\Delta P_{core,water}$ (kPa)	Q_{fuel} (kW)	Q_{water} (kW)	Q_{ave} (kW)
13	0.1957	0.3299	28.25	85.46	86.74	69.17	3.07	6.95	2.74	8.61	21.73	24.28	23.01
14	0.1955	0.3503	28.50	86.11	87.26	70.63	3.07	6.90	2.81	9.49	21.90	24.42	23.16
15	0.1957	0.3743	28.83	86.50	87.28	71.47	3.07	6.87	2.87	10.58	21.98	24.79	23.39
16	0.2750	0.1181	30.30	77.59	92.12	38.34	3.03	12.93	2.13	1.95	24.95	26.56	25.76
17	0.2513	0.1180	30.46	78.33	90.66	38.51	3.03	11.32	2.08	1.94	23.13	25.74	24.44
18	0.2361	0.1181	30.30	80.13	90.84	40.36	3.05	10.27	2.00	1.90	22.69	24.94	23.82
19	0.2204	0.1181	30.26	82.31	91.24	41.42	3.09	9.06	1.98	1.87	22.22	24.62	23.42
20	0.2038	0.1183	30.26	84.54	92.34	43.51	3.04	7.96	2.00	1.83	21.52	24.18	22.85
21	0.1884	0.1184	30.17	86.98	93.29	45.54	3.11	6.94	2.02	1.79	20.91	23.67	22.29
22	0.1720	0.1186	29.85	90.71	95.74	49.35	2.93	6.02	2.09	1.74	20.59	23.04	21.81
23	0.1556	0.1187	29.47	94.13	98.34	52.86	3.02	5.12	2.20	1.69	19.90	22.62	21.26
24	0.1403	0.1188	29.36	98.09	101.36	57.76	2.96	4.31	2.33	1.63	19.20	21.72	20.46
25	0.1243	0.1189	28.94	103.80	106.32	63.55	2.99	3.51	2.59	1.56	18.69	21.34	20.01
26	0.1084	0.1189	28.48	109.30	111.20	70.96	2.97	2.81	2.92	1.50	17.75	20.10	18.92
27	0.0924	0.1187	27.90	116.67	118.61	79.27	3.02	2.19	3.51	1.43	16.79	19.64	18.22
28	0.2214	0.1167	28.75	67.49	74.17	38.00	2.94	9.61	1.92	2.01	16.05	17.65	16.85
29	0.2211	0.1171	28.35	74.35	82.19	38.48	2.95	9.42	1.82	1.94	19.31	21.39	20.35
30	0.2218	0.1173	28.20	78.10	87.11	39.39	2.95	9.31	1.83	1.90	21.17	23.42	22.29
31	0.2215	0.1178	28.48	84.48	94.70	40.26	2.96	9.15	1.86	1.85	24.04	26.83	25.43
32	0.2204	0.1180	28.90	90.67	101.66	42.19	2.96	8.97	1.91	1.80	26.73	29.37	28.05
33	0.2205	0.1182	29.50	94.99	107.29	43.35	2.96	8.85	1.97	1.77	28.60	31.68	30.14
34	0.2208	0.1184	30.20	100.81	114.09	45.58	2.96	8.72	2.04	1.72	31.22	34.01	32.62
35	0.2202	0.1186	31.37	105.14	118.89	47.62	2.95	8.57	2.11	1.69	32.84	35.45	34.15
36	0.2201	0.1181	32.80	103.55	117.25	47.95	2.94	8.53	2.09	1.68	31.48	34.33	32.90
37	0.2198	0.0826	33.16	107.32	141.05	39.49	2.94	8.92	2.08	1.06	33.17	35.25	34.21
38	0.2197	0.0531	33.80	99.67	173.01	34.80	2.93	9.57	1.99	0.62	29.11	30.95	30.03
39	0.2356	0.1110	31.57	88.96	102.27	40.07	2.95	10.17	1.67	1.41	26.59	28.90	27.74
40	0.2356	0.1292	32.24	89.93	97.81	44.37	2.94	9.89	1.69	1.69	26.80	28.92	27.86
41	0.2357	0.1489	32.59	88.50	93.36	48.05	2.93	9.73	1.71	2.05	25.94	28.24	27.09
42	0.2355	0.1698	33.00	90.09	93.43	52.51	2.93	9.50	1.74	2.43	26.55	29.10	27.83
43	0.2354	0.1899	33.34	89.96	92.56	55.94	2.93	9.39	1.76	2.86	26.34	29.14	27.74
44	0.2353	0.2094	33.30	89.47	91.04	59.05	2.93	9.34	1.77	3.31	26.09	28.07	27.08
45	0.2358	0.2305	33.72	88.97	90.74	62.76	2.92	9.22	1.79	3.82	25.72	27.03	26.37
46	0.2356	0.2496	33.92	89.03	90.68	65.43	2.92	9.16	1.81	4.33	25.64	26.41	26.03
47	0.2356	0.2690	33.99	89.37	91.03	67.12	2.93	9.12	1.82	4.85	25.78	26.97	26.37
48	0.2355	0.2895	34.07	88.46	89.75	67.77	2.92	9.08	1.84	5.48	25.27	26.67	25.97
49	0.2352	0.3097	34.07	89.04	90.15	69.06	2.92	9.04	1.85	6.09	25.55	27.38	26.46
50	0.2353	0.3299	34.27	89.42	90.46	70.90	2.93	9.01	1.87	6.77	25.66	27.06	26.36
51	0.2354	0.3507	34.24	88.98	89.99	71.41	2.92	8.99	1.88	7.49	25.46	27.32	26.39
52	0.2352	0.3751	34.33	89.00	90.03	73.22	2.92	8.95	1.89	8.38	25.41	26.44	25.93
53	0.1294	0.0713	33.70	121.60	133.69	48.97	3.04	3.74	1.65	0.62	23.66	25.39	24.53
54	0.1139	0.0714	33.47	128.27	136.05	55.04	3.17	2.99	1.68	0.58	22.68	24.32	23.50
55	0.0981	0.0714	33.11	135.17	139.08	64.80	3.12	2.29	1.72	0.53	21.21	22.33	21.77
56	0.0820	0.0712	32.62	141.61	144.42	79.92	3.07	1.76	1.78	0.49	19.07	19.41	19.24
57	0.2343	0.1043	35.65	110.77	133.76	45.33	2.96	9.28	1.79	1.15	36.15	38.76	37.45
58	0.2343	0.1043	34.68	108.32	130.89	44.18	2.97	9.37	1.79	1.17	35.24	37.97	36.61
59	0.2345	0.1043	33.82	102.87	124.04	42.84	2.97	9.52	1.78	1.20	32.74	35.52	34.13
60	0.2348	0.1041	32.63	98.29	118.43	41.07	2.98	9.69	1.76	1.23	30.87	33.75	32.31
61	0.2350	0.1039	30.30	87.12	103.07	37.73	2.98	10.13	1.74	1.32	26.10	28.44	27.27
62	0.1954	0.1024	36.86	112.05	127.35	50.66	2.97	6.87	2.42	1.21	30.28	32.97	31.62
63	0.1951	0.1026	38.72	118.12	133.37	53.20	2.96	6.70	2.48	1.18	32.30	34.59	33.44
64	0.1950	0.1042	39.93	120.70	135.67	55.17	2.95	6.62	2.52	1.19	33.02	35.28	34.15
65	0.1949	0.1042	40.63	122.68	138.62	56.05	2.94	6.59	2.54	1.18	33.65	36.21	34.93
66	0.1948	0.1043	40.75	125.80	141.95	56.96	2.94	6.55	2.56	1.16	35.01	37.32	36.16
67	0.1949	0.1044	41.54	131.79	148.94	58.51	2.94	6.47	2.62	1.14	37.49	39.79	38.64
68	0.2503	0.1043	42.00	102.98	125.62	48.68	2.96	10.28	2.34	1.32	31.27	33.68	32.48
69	0.2270	0.1044	41.62	106.73	125.70	51.06	3.05	8.72	2.36	1.29	30.44	32.73	31.58
70	0.2026	0.1044	41.07	112.95	128.10	53.75	2.96	7.13	2.41	1.24	30.24	32.60	31.42
71	0.1796	0.1044	40.64	117.17	128.40	57.89	3.00	5.78	2.46	1.20	28.70	30.93	29.82
72	0.1541	0.1043	40.10	125.54	133.17	65.09	3.02	4.52	2.61	1.13	27.79	29.90	28.84
73	0.1313	0.1044	39.70	130.18	134.93	71.51	2.96	3.42	2.72	1.09	25.21	27.89	26.55
74	0.1075	0.1039	38.98	136.43	138.92	82.20	2.96	2.47	2.99	1.04	22.39	24.89	23.64
75	0.0834	0.1035	37.70	152.25	153.31	102.74	3.09	1.61	3.26	0.94	20.79	22.24	21.52
76	0.2358	0.1017	33.10	73.06	85.38	38.87	3.02	10.61	2.22	1.69	18.01	19.78	18.90
77	0.2353	0.1020	36.23	82.71	97.83	42.84	3.01	10.06	2.27	1.60	21.44	23.47	22.45
78	0.2346	0.1022	40.80	96.16	114.77	48.60	2.99	9.49	2.39	1.48	26.27	28.35	27.31
79	0.2338	0.1020	45.80	109.61	131.19	54.73	2.97	9.01	2.54	1.38	31.05	32.77	31.91
80	0.2333	0.1016	49.82	117.59	140.75	58.76	2.95	8.71	2.23	1.33	33.44	35.09	34.27
81	0.1944	0.1004	40.20	120.09	135.84	54.81	3.06	6.65	1.99	1.19	32.54	34.24	33.39
82	0.1944	0.1002	40.56	125.54	143.50	55.69	3.06	6.58	2.07	1.17	34.88	37.04	35.96
83	0.1944	0.1001	40.84	132.26	151.91	57.23	3.07	6.52	2.15	1.13	37.88	39.98	38.93
84	0.1943	0.0999	41.24	134.63	155.40	57.85	3.06	6.48	2.21	1.12	38.81	41.13	39.97
85	0.1941	0.0998	41.56	135.36	155.78	58.40	3.06	6.46	2.28	1.13	39.00	41.02	40.01
86	0.1943	0.1001	41.96	138.59	160.06	58.93	3.06	6.43	2.32	1.11	40.39	42.75	41.57
87	0.2353	0.1003	37.23	91.29	109.55	44.86	3.04	9.86	2.47	1.47	25.37	27.19	26.28

(*continued*)

Case No.	m_{fuel} (kg/s)	m_{water} (kg/s)	$T_{c,in}$ (°C)	$T_{c,out}$ (°C)	$T_{h,in}$ (°C)	$T_{h,out}$ (°C)	$P_{fuel,in}$ (MPa)	$\Delta P_{core,fuel}$ (kPa)	$P_{water,in}$ (MPa)	$\Delta P_{core,water}$ (kPa)	Q_{fuel} (kW)	Q_{water} (kW)	Q_{ave} (kW)
88	0.2349	0.1005	39.97	100.38	121.91	47.92	3.02	9.51	2.58	1.39	28.87	31.19	30.03
89	0.2345	0.1002	43.12	106.74	129.40	51.38	3.01	9.21	2.76	1.32	30.79	32.82	31.80
90	0.2344	0.0997	45.30	112.19	136.56	53.67	3.00	9.03	3.04	1.27	32.72	34.73	33.73
91	0.2340	0.0994	48.12	118.81	145.05	56.80	2.99	8.82	3.25	1.23	34.97	36.93	35.95
92	0.1953	0.2004	40.20	110.16	112.58	74.98	2.91	6.32	2.31	3.36	28.22	31.68	29.95
93	0.1952	0.1997	39.95	111.82	114.51	74.86	2.91	6.30	2.33	3.32	29.04	33.30	31.17
94	0.1953	0.1991	39.89	111.96	114.63	75.17	2.91	6.31	2.35	3.31	29.14	33.04	31.09
95	0.1951	0.2007	39.67	111.69	114.29	74.81	2.91	6.31	2.37	3.36	29.07	33.32	31.19
96	0.1952	0.1992	39.64	112.77	114.56	75.78	2.91	6.30	2.40	3.32	29.58	32.48	31.03
97	0.1952	0.2006	39.64	107.30	109.60	72.77	2.91	6.39	2.46	3.44	27.15	31.05	29.10
98	0.1946	0.3651	39.24	109.93	110.72	93.68	3.07	6.14	2.59	9.23	28.37	26.22	27.29
99	0.1946	0.3272	39.33	109.81	111.06	89.43	3.07	6.16	2.54	7.60	28.28	29.80	29.04
100	0.1947	0.2882	39.15	109.76	110.93	83.85	3.07	6.21	2.45	6.13	28.33	32.82	30.58
101	0.1946	0.2478	39.18	110.94	112.51	80.31	3.07	6.23	2.39	4.74	28.84	33.56	31.20
102	0.1947	0.2070	39.10	111.84	114.07	75.91	3.07	6.29	2.29	3.52	29.27	33.21	31.24
103	0.1946	0.1684	39.10	114.32	117.84	71.34	3.07	6.36	2.21	2.51	30.37	32.92	31.65
104	0.1944	0.1268	39.33	115.94	123.83	61.77	3.07	6.51	2.07	1.65	30.99	33.08	32.03
105	0.1946	0.0751	39.75	111.01	139.69	44.90	3.06	7.10	2.05	0.86	28.67	29.94	29.30

A.2. Experimental data water-water heat transfer

Case No.	m_h (kg/s)	m_c (kg/s)	$T_{h,in}$ (°C)	$T_{h,out}$ (°C)	$T_{c,in}$ (°C)	$T_{c,out}$ (°C)	$P_{h,in}$ (MPa)	ΔP_h (kPa)	$P_{c,in}$ (MPa)	ΔP_c (kPa)	Q_h (kW)	Q_c (kW)	Q_{ave} (kW)
1	0.0528	0.2011	120.25	20.70	20.50	44.26	1.96	1.06	2.09	9.12	21.99	19.95	20.97
2	0.0732	0.2014	99.58	21.59	21.43	48.24	1.89	1.53	2.13	8.90	23.88	22.54	23.21
3	0.0937	0.2019	86.43	22.10	21.82	50.21	1.84	2.04	2.15	8.77	25.19	23.92	24.56
4	0.1127	0.2021	76.74	22.53	22.10	50.76	1.81	2.55	2.15	8.64	25.53	24.17	24.85
5	0.1323	0.2025	70.58	23.23	22.30	52.41	1.79	3.09	2.17	8.50	26.16	25.45	25.80
6	0.1531	0.2027	65.31	24.08	22.40	52.97	1.78	3.70	2.17	8.40	26.36	25.86	26.11
7	0.1752	0.2029	61.72	25.51	22.60	54.21	1.78	4.38	2.18	8.27	26.50	26.78	26.64
8	0.1945	0.2030	59.86	26.66	22.66	54.63	1.78	4.98	2.18	8.16	26.96	27.10	27.03
9	0.2164	0.2030	57.53	28.11	22.76	53.90	1.79	5.76	2.17	8.11	26.58	26.39	26.49
10	0.2333	0.2032	56.74	29.22	22.64	53.71	1.80	6.39	2.17	8.06	26.80	26.35	26.58
11	0.2533	0.2033	55.96	30.66	22.80	53.68	1.81	7.20	2.17	8.00	26.76	26.21	26.48
12	0.2729	0.2033	55.98	31.88	22.80	53.80	1.83	8.00	2.17	7.96	27.47	26.31	26.89
13	0.2935	0.2035	55.42	33.19	22.90	53.70	1.85	8.90	2.17	7.90	27.25	26.16	26.70
14	0.1214	0.0535	107.21	69.01	19.70	105.51	2.75	1.66	2.73	0.67	19.46	19.19	19.32
15	0.1197	0.2064	74.84	23.20	22.62	51.35	1.73	2.71	2.04	8.77	25.82	24.76	25.29
16	0.1195	0.2329	74.97	23.50	23.06	47.94	1.72	2.75	2.02	10.72	25.70	24.20	24.95
17	0.1195	0.2591	75.12	23.80	23.40	45.85	1.71	2.76	2.02	12.80	25.62	24.29	24.95
18	0.1195	0.2860	75.22	23.95	23.70	44.70	1.71	2.77	2.02	14.96	25.59	25.07	25.33
19	0.1194	0.3128	75.31	24.20	23.90	44.22	1.70	2.78	2.02	17.30	25.50	26.54	26.02
20	0.1194	0.3398	75.78	24.50	24.25	43.31	1.70	2.78	2.02	19.77	25.59	27.04	26.31
21	0.1195	0.3667	75.93	24.80	24.55	42.37	1.70	2.78	2.02	22.25	25.52	27.27	26.40
22	0.1195	0.3940	76.13	25.02	24.80	41.90	1.70	2.79	2.02	24.87	25.51	28.12	26.82
23	0.1194	0.4394	76.33	25.40	25.15	40.67	1.69	2.79	2.03	29.55	25.41	28.48	26.95
24	0.1195	0.4663	76.78	25.50	25.30	39.98	1.69	2.78	2.04	32.41	25.60	28.56	27.08
25	0.1098	0.2079	75.76	22.20	21.80	48.30	1.63	2.48	1.81	8.28	24.56	23.00	23.78
26	0.1089	0.2084	82.68	23.00	22.60	51.99	1.65	2.40	1.86	8.18	27.16	25.57	26.36
27	0.1093	0.2088	88.41	23.81	23.43	55.91	1.66	2.36	1.91	8.12	29.51	28.31	28.91
28	0.1096	0.2092	94.84	24.58	24.15	59.60	1.68	2.32	1.97	8.01	32.20	30.96	31.58
29	0.1098	0.2095	100.33	25.53	25.10	62.91	1.70	2.28	2.03	7.96	34.34	33.08	33.71
30	0.1103	0.2098	106.88	26.42	25.95	66.89	1.72	2.24	2.11	7.89	37.14	35.86	36.50
31	0.1105	0.2099	109.60	26.95	26.50	68.46	1.72	2.22	2.15	7.85	38.23	36.78	37.50

Data availability

Data will be made available on request.

References

[1] L. Chai, S.A. Tassou, A review of printed circuit heat exchangers for helium and supercritical CO2 Brayton cycles, Therm. Sci. Eng. Prog. 18 (2020) 22.

[2] I.H. Kim, H.C. No, Physical model development and optimal design of PCHE for intermediate heat exchangers in HTGRs, Nucl. Eng. Des. 243 (2012) 243–250.

[3] Q. Zhu, X. Tan, B. Barari, M. Caccia, A.R. Strayer, M. Pishahang, K.H. Sandhage, A. Henry, Design of a 2 MW ZrC/W-based molten-salt-to-sCO2 PCHE for concentrated solar power, Appl. Energy 300 (2021).

[4] F. Jin, D. Chen, L. Hu, Y. Huang, S. Bu, Optimization of zigzag parameters in printed circuit heat exchanger for supercritical CO2 Brayton cycle based on multi-objective genetic algorithm, Energy Convers. Manag. 270 (2022).

[5] M. Saeed, A. Ali Awais, A.S. Berrouk, CFD aided design and analysis of a precooler with zigzag channels for supercritical CO2 power cycle, Energy Convers. Manag. 236 (2021).

[6] H. Zhang, L. Shi, W. Xuan, T. Chen, Y. Li, H. Tian, G. Shu, Analysis of printed circuit heat exchanger (PCHE) potential in exhaust waste heat recovery, Appl. Therm. Eng. 204 (2022).

[7] B. Liu, M. Lu, B. Shui, Y. Sun, W. Wei, Thermal-hydraulic performance analysis of printed circuit heat exchanger precooler in the Brayton cycle for supercritical CO2 waste heat recovery, Appl. Energy 305 (2022).

[8] S. Baek, G. Hwang, S. Jeong, J. Kim, Development of compact heat exchanger for LNG FPSO, in: ISOPE International Ocean and Polar Engineering Conference, ISOPE, 2011 pp. ISOPE-I-11-334.

[9] Z. Guo, Y. Zhao, Y. Zhu, F. Niu, D. Lu, Optimal design of supercritical CO2 power cycle for next generation nuclear power conversion systems, Prog. Nucl. Energy 108 (2018) 111–121.

[10] H. Chang, J. Lian, T. Ma, L. Li, Q. Wang, Design and optimization of an annular air-hydrogen precooler for advanced space launchers engines, Energy Convers. Manag. 241 (2021).

[11] Y. Fu, W. Liu, H. Qi, Q. Chen, J. Wen, G. Xu, Heat transfer area optimization of intermediate heat-exchange cycle system for aero engines, Int. J. Heat Mass Transf. 220 (2024).

[12] W. Liu, G. Xu, X. Gang, H. Qi, M. Li, J. Wen, Y. Fu, Theoretical modeling, experimental validation, and thermodynamic analysis on intermediate heat-exchange cycle system, Int. Commun. Heat Mass Transf. 156 (2024).

[13] Y. Cheng, Y. Li, J. Wang, L. Tam, Y. Chen, Q. Wang, T. Ma, Multi-objective optimization of printed circuit heat exchanger used for hydrogen cooler by exergoeconomic method, Energy 262 (2023).

[14] M. Chen, X. Sun, R.N. Christensen, S. Shi, I. Skavdahl, V. Utgikar, P. Sabharwall, Experimental and numerical study of a printed circuit heat exchanger, Ann. Nucl. Energy 97 (2016) 221–231.

[15] S. Liu, Y. Huang, J. Wang, R. Liu, J. Zang, Experimental study of thermal-hydraulic performance of a printed circuit heat exchanger with straight channels, Int. J. Heat Mass Transf. 160 (2020).

[16] J.-W. Seo, Y.-H. Kim, D. Kim, Y.-D. Choi, K.-J. Lee, Heat transfer and pressure drop characteristics in straight microchannel of printed circuit heat exchangers, Entropy 17 (5) (2015) 3438–3457.

[17] T.L. Ngo, Y. Kato, K. Nikitin, T. Ishizuka, Heat transfer and pressure drop correlations of microchannel heat exchangers with S-shaped and zigzag fins for carbon dioxide cycles, Exp. Thermal Fluid Sci. 32 (2) (2007) 560–570.

[18] I.H. Kim, H.C. No, Thermal hydraulic performance analysis of a printed circuit heat exchanger using a helium–water test loop and numerical simulations, Appl. Therm. Eng. 31 (17–18) (2011) 4064–4073.

[19] I.H. Kim, H.C. No, Thermal–hydraulic physical models for a printed circuit heat exchanger covering He, He–CO2 mixture, and water fluids using experimental data and CFD, Exp. Thermal Fluid Sci. 48 (2013) 213–221.

[20] S.-J. Yoon, J. O'Brien, M. Chen, P. Sabharwall, X. Sun, Development and validation of Nusselt number and friction factor correlations for laminar flow in semi-circular zigzag channel of printed circuit heat exchanger, Appl. Therm. Eng. 123 (2017) 1327–1344.

[21] A. Katz, S.R. Aakre, M.H. Anderson, D. Ranjan, Experimental investigation of pressure drop and heat transfer in high temperature supercritical CO2 and helium in a printed-circuit heat exchanger, Int. J. Heat Mass Transf. 171 (2021) 19.

[22] F. Jin, D. Yuan, D. Chen, L. Hu, Y. Huang, S. Bu, Experimental study on cooling heat transfer performance of supercritical CO2 in zigzag printed circuit heat exchanger, Int. J. Heat Mass Transf. 215 (2023).

[23] M. Qu, Y. Zhang, X. Zhang, H. Mu, W. Fan, X. Chen, Q. Tan, Numerical analysis of the effect of wave amplitude on thermohydraulic performance in a heat exchanger with sinusoidal wavy channels, Int. Commun. Heat Mass Transf. 155 (2024).

[24] A.O. Samarmad, H.M. Jaffal, Examining the effect of backward/forward-facing wavy channels on the thermohydraulic performance of a printed circuit heat exchanger under the laminar flow regime, Int. J. Thermofluids 20 (2023).

[25] A. Oleiwi Samarmad, H. Mohammad Jaffal, Performance evaluation of a printed circuit heat exchanger with a novel two-way corrugated channel, Results Eng. 19 (2023).

[26] W. Wang, B. Li, Y. Tan, B. Li, Y. Shuai, Multi-objective optimal design of NACA airfoil fin PCHE recuperator for micro-gas turbine systems, Appl. Therm. Eng. 204 (2022).

[27] S. Chung, S.W. Lee, N. Kim, S.M. Shin, M.H. Kim, H. Jo, Experimental study of printed-circuit heat exchangers with airfoil and straight channels for optimized recuperators in nitrogen Brayton cycle, Appl. Therm. Eng. 218 (2023).

[28] C.-Y. Chou, G.-C. Kuo, C.-C. Chueh, Numerical analysis of thermal-hydraulic influence of geometric flow baffles on multistage Tesla valves in printed circuit heat exchangers, Appl. Therm. Eng. 251 (2024).

[29] Z. Li, D. Lu, X. Wang, Q. Cao, Analysis on the flow and heat transfer performance of SCO2 in airfoil channels with different structural parameters, Int. J. Heat Mass Transf. 219 (2024).

[30] L. Tang, Z. Cao, J. Pan, Investigation on the thermal-hydraulic performance in a PCHE with airfoil fins for supercritical LNG near the pseudo-critical temperature under the rolling condition, Appl. Therm. Eng. 175 (2020).

[31] J.H. Park, M.H. Kim, Experimental investigation on comprehensive thermal-hydraulic performance of supercritical CO2 in a NACA 0020 airfoil fin printed circuit heat exchanger, Int. J. Heat Mass Transf. 220 (2024).

[32] H. Chang, Z. Han, X. Li, T. Ma, Q. Wang, Experimental investigation on heat transfer performance based on average thermal-resistance ratio for supercritical carbon dioxide in asymmetric airfoil-fin printed circuit heat exchanger, Energy 254 (2022).

[33] Y. Yang, H. Li, B. Xie, L. Zhang, Y. Zhang, Experimental study of the flow and heat transfer performance of a PCHE with rhombic fin channels, Energy Convers. Manag. 254 (2022).

[34] S.R. Pidaparti, M.H. Anderson, D. Ranjan, Experimental investigation of thermal-hydraulic performance of discontinuous fin printed circuit heat exchangers for supercritical CO2 power cycles, Exp. Thermal Fluid Sci. 106 (2019) 119–129.

[35] E. Wilson, A basis for rational design of heat transfer apparatus, J. Fluids Eng. 37 (1915) 47–70.

[36] J.W. Rose, Heat-transfer coefficients, Wilson plots and accuracy of thermal measurements, Exp. Thermal Fluid Sci. 28 (2–3) (2004) 77–86.

[37] J.H. Park, J.G. Kwon, T.H. Kim, M.H. Kim, J.-E. Cha, H. Jo, Experimental study of a straight channel printed circuit heat exchanger on supercritical CO2 near the critical point with water cooling, Int. J. Heat Mass Transf. 150 (2020).

[38] J.-H. Shin, K.H. Lee, S.H. Yoon, Experimental work for the performance of a printed circuit heat exchanger (PCHE) using nitrogen under trans-critical states, Energy Rep. 8 (2022) 12765–12775.

[39] Z. Han, J. Guo, J. Chen, X. Huai, Experimental and numerical investigations on thermal-hydraulic characteristics of supercritical CO2 flows in printed circuit heat exchangers, Int. J. Therm. Sci. 194 (2023).

[40] S. Baik, S.G. Kim, J. Lee, J.I. Lee, Study on CO2 – water printed circuit heat exchanger performance operating under various CO₂ phases for S-CO2 power cycle application, Appl. Therm. Eng. 113 (2017) 1536–1546.

[41] W.-Q. Wang, Y. Qiu, Y.-L. He, H.-Y. Shi, Experimental study on the heat transfer performance of a molten-salt printed circuit heat exchanger with airfoil fins for concentrating solar power, Int. J. Heat Mass Transf. 135 (2019) 837–846.

[42] H.-Y. Shi, M.-J. Li, W.-Q. Wang, Y. Qiu, W.-Q. Tao, Heat transfer and friction of molten salt and supercritical CO2 flowing in an airfoil channel of a printed circuit heat exchanger, Int. J. Heat Mass Transf. 150 (2020).

[43] Z. Han, J. Guo, H. Zhang, J. Chen, X. Huai, X. Cui, Experimental and numerical studies on novel airfoil fins heat exchanger in flue gas heat recovery system, Appl. Therm. Eng. 192 (2021).

[44] E. Nourafkan, G. Karimi, J. Moradgholi, Experimental study of laminar convective heat transfer and pressure drop of cuprous oxide/water nanofluid inside a circular tube, Exp. Heat Transf. 28 (1) (2014) 58–68.

[45] H. Deng, C. Zhang, G. Xu, B. Zhang, G. Liu, Density measurements of endothermic hydrocarbon fuel at sub-and supercritical conditions, J. Chem. Eng. Data 56 (6) (2011) 2980–2986.

[46] H. Deng, C. Zhang, G. Xu, B. Zhang, Z. Tao, K. Zhu, Viscosity measurements of endothermic hydrocarbon fuel from (298 to 788) K under supercritical pressure conditions, J. Chem. Eng. Data 57 (2) (2012) 358–365.

[47] H. Deng, K. Zhu, G. Xu, Z. Tao, C. Zhang, G. Liu, Isobaric specific heat capacity measurement for kerosene RP-3 in the near-critical and supercritical regions, J. Chem. Eng. Data 57 (2) (2012) 263–268.

[48] G. Xu, Z. Jia, J. Wen, H. Deng, Y. Fu, Thermal-conductivity measurements of aviation kerosene RP-3 from (285 to 513) K at sub-and supercritical pressures, Int. J. Thermophys. 36 (4) (2015) 620–632.

[49] I.H. Bell, J. Wronski, S. Quoilin, V. Lemort, Pure and pseudo-pure fluid thermophysical property evaluation and the open-source thermophysical property library CoolProp, Ind. Eng. Chem. Res. 53 (6) (2014) 2498–2508.

[50] W. Liu, G. Xu, Y. Fu, J. Wen, N. Zhang, Numerical investigation on forced, natural, and mixed convective heat transfer of n-decane in laminar flow at supercritical pressures, Int. J. Heat Mass Transf. 209 (2023).

[51] I.E. Idelchik, Handbook of Hydraulic Resistance, Washington, 1986.

[52] Y. Fu, B. Bian, Y. Liu, L. Zhang, M. Li, J. Wen, G. Xu, Airside heat transfer analysis using Wilson plot method of three analogous serpentine tube heat exchangers for aero-engine cooling, Appl. Therm. Eng. 248 (2024).

[53] J. Wen, Y. Fu, X. Bao, Y. Liu, G. Xu, Flow resistance and convective heat transfer performances of airflow through helical-tube bundles, Int. J. Heat Mass Transf. 130 (2019) 778–786.

[54] Y. Fu, W. Liu, J. Wang, L. Zhang, J. Wen, H. Wu, G. Xu, Experimental investigation on heat transfer enhancement of supercritical pressure aviation kerosene in tubular laminar flow by vibration, Appl. Therm. Eng. 257 (2024).

[55] H. Deng, C. Zhang, G. Xu, Z. Tao, K. Zhu, Y. Wang, Visualization experiments of a specific fuel flow through quartz-glass tubes under both sub- and supercritical conditions, Chin. J. Aeronaut. 25 (3) (2012) 372–380.

[56] J.J. Moré, The Levenberg-Marquardt algorithm: implementation and theory, in: Numerical analysis: proceedings of the biennial Conference held at Dundee, June 28–July 1, 1977, Springer, 2006, pp. 105–116.

[57] S.-H. Liu, Y.-P. Huang, J.-F. Wang, R.-L. Liu, Experimental study on transitional flow in straight channels of printed circuit heat exchanger, Appl. Therm. Eng. 181 (2020).

[58] F. Dittus, L. Boelter, Heat transfer in automobile radiators of the tubular type, Int. Commun. Heat Mass Transf. 12 (1) (1985) 3–22.

[59] N. Tsuzuki, M. Utamura, T.L. Ngo, Nusselt number correlations for a microchannel heat exchanger hot water supplier with S-shaped fins, Appl. Therm. Eng. 29 (16) (2009) 3299–3308.